Sphingolipid long-chain base hydroxylation influences plant growth and callose deposition in *Physcomitrium patens*

Jasmin Gömann[1], **Cornelia Herrfurth**[1,2] (iD), **Agnieszka Zienkiewicz**[1] (iD), **Till Ischebeck**[1,3] (iD), **Tegan M. Haslam**[1] (iD), **Ellen Hornung**[1] and **Ivo Feussner**[1,2,3] (iD)

[1]Department of Plant Biochemistry, Albrecht-von-Haller-Institute for Plant Sciences, University of Göttingen, Göttingen D-37077, Germany; [2]Service Unit for Metabolomics and Lipidomics, Göttingen Center for Molecular Biosciences (GZMB), University of Göttingen, Göttingen D-37077, Germany; [3]Department of Plant Biochemistry, Göttingen Center for Molecular Biosciences (GZMB), University of Göttingen, Göttingen D-37077, Germany

Summary

• Sphingolipids are enriched in microdomains in the plant plasma membrane (PM). Hydroxyl groups in the characteristic long-chain base (LCB) moiety might be essential for the interaction between sphingolipids and sterols during microdomain formation. Investigating LCB hydroxylase mutants in *Physcomitrium patens* might therefore reveal the role of certain plant sphingolipids in the formation of PM subdomains.

• *Physcomitrium patens* mutants for the LCB C-4 hydroxylase *S4H* were generated by homologous recombination. Plants were characterised by analysing their sphingolipid and steryl glycoside (SG) profiles and by investigating different gametophyte stages.

• *s4h* mutants lost the hydroxyl group at the C-4 position of their LCB moiety. Loss of this hydroxyl group caused global changes in the moss sphingolipidome and in SG composition. Changes in membrane lipid composition may trigger growth defects by interfering with the localisation of membrane-associated proteins that are crucial for growth processes such as signalling receptors or callose-modifying enzymes.

• Loss of LCB-C4 hydroxylation substantially changes the *P. patens* sphingolipidome and reveals a key role for S4H during development of nonvascular plants. *Physcomitrium patens* is a valuable model for studying the diversification of plant sphingolipids. The simple anatomy of *P. patens* facilitates visualisation of physiological processes in biological membranes.

Introduction

Sphingolipids are involved in essential cellular and subcellular processes in eukaryotes and some prokaryotes (Smith & Merrill, 2002; Lynch & Dunn, 2004; Sperling *et al.*, 2005). As abundant lipid molecules, their predominant role is to maintain the structural integrity of the plasma membrane (PM) and of endomembrane systems. Their amphipathic nature arises from their unique hydrophobic sphingoid backbone that is connected to hydrophilic head groups (Lynch & Dunn, 2004). The backbone contains an *N*-acylated amino alcohol, also known as long-chain base (LCB). LCBs are characteristic for sphingolipids and therefore define them as a distinct lipid class. Sphingolipids account for *c.* 40 mol% of PM lipids in plants (Sperling *et al.*, 2005; Cacas *et al.*, 2016) and are thought to play a key role in membrane organisation by participating in microdomain and nanodomain formation. In addition to their structural role, some sphingolipids act as signalling molecules in several processes including programmed cell death (PCD) (Liang *et al.*, 2003; Shi *et al.*, 2007; Zienkiewicz *et al.*, 2020) and responses to biotic and abiotic stress (Huby *et al.*, 2020). They, furthermore, play a role

as necrosis and ethylene-inducing peptide 1-like toxin receptors during plant–pathogen interactions (Lenarčič *et al.*, 2017).

The plant sphingolipidome can be broken down into four classes: LCBs (0.5% of *Arabidopsis thaliana* leaf sphingolipids), ceramides (2%), glycosylceramides (GlcCers) (34%) and glycosyl inositolphosphorylceramides (GIPCs) (64%) (Markham *et al.*, 2006; Markham & Jaworski, 2007). Sphingolipid biosynthesis starts in the endoplasmic reticulum (ER) with the condensation of palmitoyl-CoA and serine forming 3-ketosphinganine. This sphingoid precursor is reduced to the LCB sphinganine, also called dihydroxy LCB or d18:0. Plant LCBs typically have a hydrocarbon chain length of 18 carbon atoms. The LCBs are the core structures of ceramides and complex sphingolipids and can be *N*-acylated through the action of ceramide synthases. *N*-acylation of LCBs to long-chain fatty acids (LCFAs) or very long-chain fatty acids (VLCFAs) produces ceramides. In plants, the pool of acyl chain lengths of sphingolipids typically ranges from 16 to 26 carbons. Complex sphingolipids (GlcCers and GIPCs) are generated through the attachment of a polar head group to the C-1 position of the LCB. Sphingolipids are a diverse lipid class, in part due to structural modifications on their LCB or fatty acid moiety. These

include phosphorylation, hydroxylation and desaturation and are usually introduced at the level of LCBs, acyl-CoAs or ceramides. Even small modifications have a great effect on the biophysical properties of sphingolipids (Resemann *et al.*, 2021).

Most of our knowledge of plant sphingolipid metabolism has been gained from studying the vascular model *A. thaliana*. Many enzymes in the sphingolipid pathway have been thoroughly investigated, and a multitude of mutants with severe, pleiotropic phenotypes have been identified (Luttgeharm *et al.*, 2016). However, the tissue and organ complexity of vascular plants has made it difficult to assign distinct functions to specific sphingolipid molecules. Furthermore, many *A. thaliana* sphingolipid mutants are embryo lethal or severely dwarfed, making it challenging or impossible to perform phenotypic characterisation on true knockout plants (Msanne *et al.*, 2015; Tartaglio *et al.*, 2017; Gonzalez Solis *et al.*, 2020).

The moss *Physcomitrium patens* is an appealing alternative model. The anatomical simplicity of moss organs greatly facilitates visualisation of intercellular and intracellular processes. Additionally, *P. patens* can be propagated vegetatively, meaning that mutants that do not reach reproductive maturity can still be investigated. Bryophytes and vascular plants diverged early in land plant evolution, *c.* 450 Ma (Rensing *et al.*, 2008). Studying this bryophyte model will therefore complement work in vascular plant models to provide insight into conserved features of land plants. A recent study described the lipidome of *P. patens*, including glycerolipids, sterols and sphingolipids (Resemann *et al.*, 2021), and revealed that sphingolipid metabolism is fundamentally conserved between nonvascular and vascular plants. An overview of the *P. patens* sphingolipid metabolism is depicted in Fig. 1 summarised from (Cacas *et al.*, 2013; Luttgeharm *et al.*, 2016; Resemann *et al.*, 2021).

One essential modification of plant sphingolipids is the hydroxylation of the LCB and fatty acid moieties. Following its formation, the LCB moiety contains two hydroxyl groups and is called dihydroxy LCB. The C-1 and C-3 hydroxyl groups result from the precursor molecules serine and palmitoyl-CoA, respectively (Dunn *et al.*, 2004; Lynch & Dunn, 2004). A hallmark of plant and yeast sphingolipids is a third hydroxyl group added to C-4 of the LCB moiety by an LCB hydroxylase (Haak *et al.*, 1997; Sperling *et al.*, 2001; Markham *et al.*, 2006; Chen *et al.*, 2008). This LCB moiety is referred to as trihydroxy LCB. Overall, *c.* 90% of all LCB moieties found in total leaf extract from *A. thaliana* contain trihydroxy LCBs (Markham *et al.*, 2006; Tarazona *et al.*, 2015). Trihydroxy LCBs are mainly acylated to VLCFAs and channelled into the GIPC pool (Buré *et al.*, 2011).

GIPCs are the most abundant plant sphingolipids and account for *c.* 64% of total sphingolipids in *A. thaliana* leaves (Markham *et al.*, 2006). GIPCs make up 30–40 mol% of the plasma membrane (PM) lipids of *Nicotiana tabacum* and 60–80% of the total outer leaflet lipids (Cacas *et al.*, 2016). The presence of additional hydroxyl groups in the sphingoid backbone allows sphingolipids to form more hydrogen bonds with other membrane components such as sterols and saturated phospholipids; this interaction affects the biophysical properties of the membrane (Quinn & Wolf, 2009; Klose *et al.*, 2010; Mamode Cassim *et al.*, 2019).

Membrane fractions enriched in sterols and sphingolipids, especially GIPCs, form stable gel phases with increased melting temperatures, so-called liquid-ordered domains or lipid rafts (Simons & Ikonen, 1997; Pike, 2009). These domains serve as protein-sorting platforms in the PM (Simons & Ikonen, 1997; de Almeida *et al.*, 2003; Huang *et al.*, 2019). *Arabidopsis thaliana* mutants with altered GIPC content show severe growth and developmental phenotypes, which could be caused by defects in cytokinesis, involving altered cell plates and impaired plasmodesmal cell-to-cell transport (Chen *et al.*, 2008; Molino *et al.*, 2014; Liu *et al.*, 2020; Yan & Liu, 2020). GIPCs are therefore thought to orchestrate membrane dynamics during plant development.

Although the presence of three hydroxyl groups in the LCB moiety is considered a characteristic and crucial feature for plants, sphingolipid C-4 hydroxylases have only been characterised in *A. thaliana* (Sperling *et al.*, 2001; Chen *et al.*, 2008). *Arabidopsis thaliana* SPHINGOID BASE HYDROXYLASE1 (*At*SBH1) and *At*SBH2 are functionally redundant LCB C-4 hydroxylases. Only *sbh1 sbh2* double mutants completely lack trihydroxy LCBs, affecting the overall sphingolipid content. Null mutants were severely dwarfed, were impaired in cell expansion and division, and failed to transition from vegetative to reproductive development. LCB C-4 hydroxylation was therefore deemed essential for *A. thaliana* growth and viability.

The following study shows the significance of the t18:0 LCB moiety in sphingolipid metabolism in *P. patens*. By generating a loss-of-function mutant of the single gene *sphinganine C-4 hydroxylase* (*S4H*) via homologous recombination, a complete loss of t18:0 LCB-containing sphingolipids was achieved. This loss resulted in global changes across all sphingolipid classes. Expression of *Pp*S4H in the *Saccharomyces cerevisiae* LCB C-4 hydroxylase knockout mutant *sur2Δ* restored the formation of t18:0 LCB-containing sphingolipids in yeast. Similar to the *A. thaliana sbh1 sbh2* mutant, the *P. patens s4h* mutants showed severely stunted growth in all developmental stages. This growth phenotype might be attributed to impaired cytokinesis, as indicated by altered deposition of the cell plate marker callose. This study highlights the advantages of *P. patens* as a model plant for investigating the role of sphingolipids in membrane dynamics.

Materials and Methods

Plant material and growth conditions

The 'Gransden' wild-type strain of *P. patens* (Hedw.) Bruch & Schimp was used. Plant material was grown at 25°C, in 16 h : 8 h, light : dark cycle, with a photon flux of 50–70 µmol $m^{-2} s^{-1}$. Protonema material was cultivated weekly on BCD agar medium plates (90 mm diameter) containing 1 mM $CaCl_2$ and 5 mM ammonium tartrate (BCDAT) (Ashton & Cove, 1977) and covered with sterile cellophane discs (Folia, Wendelstein, Germany). Regular maintenance was achieved by collecting 1- to 2-wk-old protonema tissue, disrupting the tissue for 20 s using a tissue lyser (Ultra Turrax; Ika, Staufen, Germany) and spreading the material onto fresh medium plates. For lipidomics and growth measurements, the dry mass of each
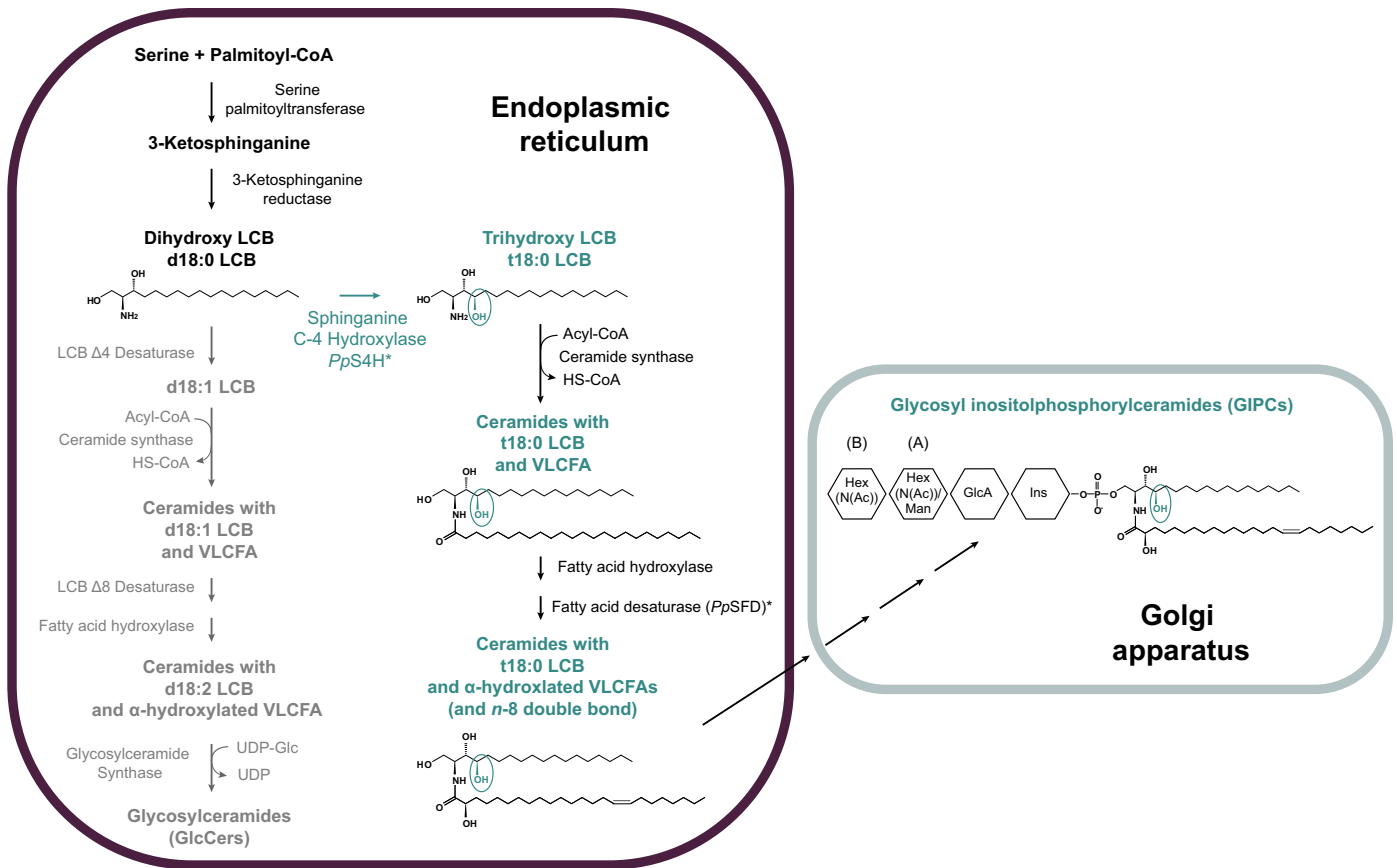
Fig. 1 Trihydroxy sphingolipids are mainly channelled into GIPC formation in *P. patens*. The depicted sphingolipid metabolism shows the two pathways for glycosylceramide (GlcCer) and glycosyl inositolphosphorylceramide (GIPC) synthesis in *P. patens*. Dihydroxy long-chain bases (LCBs) are channelled into GlcCer formation (grey) and trihydroxy LCBs are channelled into GIPC formation (blue). GIPC species with one additional hexose moiety are called series A GIPCs and GIPC species with two additional hexose moieties are called series B GIPCs. Asterisks indicate functionally characterised enzymes in *P. patens*. GlcA, glucuronic acid; Hex, hexose; HexNAc, *N*-acetylhexosamine; HS-CoA, coenzyme A; Ins, inositol; Man, mannose; SFD, sphingolipid fatty acid desaturase; UDP-Glc, uridine diphosphate glucose; VLCFA, very long-chain fatty acid.

genotype inoculated was normalised. Protonema material was harvested after 10 d of growth, weighed for fresh weight (FW) biomass determination and frozen in liquid nitrogen. Collected tissue was lyophilised and weighed again for dry weight (DW) determination. To obtain enough material for analysis, the tissue from eight plates was pooled during each cultivation round.

To image protonemal development, a *c.* 1 mm spot inocula of 1- to 2-wk-old protonemata were placed on plates containing BCD medium with 1 mM CaCl₂. For induction of gametophores, spot inocula were incubated on BCD medium plates for 5–6 wk.

For targeted cultivation of skotonema filaments, spot inocula were placed on square Petri dishes containing BCDAT medium with 2% (w/v) sucrose and were grown horizontally for 1 wk under continuous light. Plates were subsequently shifted into the vertical position and grown in the dark for another 3–4 wk.

Images were taken with a binocular microscope (Olympus SZX12 binocular; Olympus Corpo., Tokyo, Japan) linked to a digital camera (R6 Retiga; QImaging, Surrey, Canada). Photographs were acquired using Ocular Image Acquisition Software (v.1.0; Digital Optics Ltd, Auckland, New Zealand).

Images were processed using ImageJ 1.52b software (Schneider *et al.*, 2012).

Generation of targeted knockout plasmids

To construct the vector for targeted knockout of the *S4H* gene, 750-bp genomic DNA fragments of the 5′ region and the 3′ region of *S4H* were amplified (Supporting information Table S1). These fragments were cloned into a pBluescript vector flanking a kanamycin cassette driven by the 35S promotor. Correct cloning of the fragments into the destination vector was confirmed by sequencing. Before transformation, the fragment containing flanking regions and the kanamycin cassette was excised using restriction enzymes *Apa*I and *Xba*I.

Physcomitrium patens transformation and molecular characterisation of knockout mutants

Before transformation, protonema material was cultured in nonaerated, shaking liquid cultures in sterile flasks in Knop medium (Reski & Abel, 1985). At 1 wk before transformation,

the plant material was transferred to liquid Knop medium containing $1:10$ original $Ca(NO_3)_2$ amount. Polyethylene glycol (PEG)-mediated transformation followed (Schaefer *et al.*, 1991).

Molecular characterisation of targeted gene disruption

A small explant of regenerated protonemata was used for DNA isolation using the cetyl trimethylammonium bromide (CTAB) extraction method. Integration of the kanamycin cassette into *P. patens* was prescreened using a primer pair that was specific for the selection cassette (Table S2). Subsequently, insertion of the selection cassette into the correct locus was confirmed using a primer pair specific for the selection cassette and the corresponding $5'$ and $3'$ untranslated regions of *S4H* (Table S2).

Reverse transcriptase PCR for mutant characterisation

Total RNA was extracted from wild-type and mutant tissue using TRIzol™ reagent (Thermo Fisher Scientific, Waltham, MA, USA). Before cDNA synthesis, RNA was treated with DNaseI (Thermo Fisher Scientific) according to the manufacturer's instructions; 1 µg of DNA-free RNA was applied for cDNA synthesis using the RevertAid H Minus First Strand cDNA Synthesis Kit (Thermo Fisher Scientific). *S4H* and *ACTIN8* specific primers are listed in Table S3.

Particle bombardment of *P. patens* protonema cells for sub-cellular localisation

Physcomitrium patens wild-type protonemata were grown on BCD medium covered with cellophane for 10 d before the particle bombardment. The gold particles used for the bombardment assay were prepared and precipitated as described in Mueller *et al.* (2017). The Pp*S4H* coding sequence was amplified from *P. patens* cDNA and was cloned into a pEntry vector system (pUC18-derived) under a 35S promoter and with a C-terminal eYFP tag using the primers listed in Table S4. The used *mCerulean::KDEL* ER marker plasmid was described in Müller *et al.* (2015) and was kindly provided by Ralf Reski, Freiburg (Mueller & Reski, 2015). Next, 5–8 µg of plasmid DNA were precipitated onto the gold particles by mixing with 0.1 M spermidine and 2.5 M $CaCl_2$. The mixture was vigorously vortexed for 1 min. Particles were subsequently washed with 100% ethanol and finally resuspended in 24 µl 100% ethanol. *P. patens* protonemata were bombarded using a particle gun (PDS-1000/He; Bio-Rad, Hercules, CA, USA) with 900 psi rupture discs; 6 µl of the gold particles were pipetted onto the macro carrier. The rupture discs were assembled two levels above the macro carrier with the gold particles and the protonemata were located two levels below the gold. After bombardment the protonemata were incubated under normal conditions for 48 h before visualisation using confocal laser scanning microscopy.

Heterologous expression in *S. cerevisiae* LCB C-4 knockout mutant *sur2Δ*

The *P. patens S4H* gene was synthesised and codon usage optimised for *S. cerevisiae* expression (GenScript, Piscataway Township, NJ, USA) and cloned into the pYES2-CT vector (Thermo Fisher Scientific) using the primers listed in Table S5. Successful cloning was confirmed by sequencing. The empty vector and the *S4H*-containing plasmid were transformed into the *sur2Δ*-null mutant (Haak *et al.*, 1997) using the LiAc/SS carrier DNA/PEG method according to Gietz & Schiestl (2007). Transformed yeast and the corresponding wild-type strain (BY4741) were precultured for 24 h in synthetic dropout (SD) medium lacking uracil and containing 2% glucose. For gene induction, yeast main cultures were inoculated to a final OD_{600} of 0.02 in SD lacking uracil and containing 2% galactose and 2% raffinose and grown for another 24 h. Yeast cultures were incubated at 30°C in shaking flasks. Cells were harvested at 3000 *g* for 10 min, washed with water and stored at −80°C. Yeast cells were lyophilised before lipid extraction and analysis.

Lipid extraction

The monophasic lipid extraction of Markham *et al.* (2006) was followed with minor modifications; 20 mg lyophilised and homogenised *P. patens* or *S. cerevisiae* material were immersed in a 60°C preheated solvent mixture containing propan-2-ol : hexane : water $(60:26:14,v/v/v)$. The mixture was incubated for 30 min at 60°C with vortexing every 10 min. The solution was centrifuged and the supernatant collected and evaporated under a stream of nitrogen. Dried lipids were dissolved in 800 µl tetrahydrofuran : methanol : water $(4:4:1,v/v/v)$. Extracts were directly applied for LCB measurement using ultraperformance liquid chromatography (UPLC) coupled with nanoelectrospray ionisation (nanoESI) and triple quadrupole tandem mass spectrometry (MS/MS) (UPLC-nanoESI-MS/MS) analysis (AB Sciex) or processed further as described in the following section.

Methylamine treatment

For ceramide and GlcCer analysis, 50 µl of the lipid extract were evaporated; 1.4 ml 33% (w/v) methylamine in ethanol together with 600 µl H_2O were added to the dried extract (Markham & Jaworski, 2007). After methylamine treatment the solvent was evaporated, dried lipids were dissolved in 50 µl tetrahydrofuran : methanol : water $(4:4:1,v/v/v)$ for UPLC-nanoESI-MS/MS.

Derivatisation with acetic anhydride

Acetic anhydride treatment for detection of LCB phosphates (LCB-Ps) was performed according to (Berdyshev *et al.*, 2005; Yanagawa *et al.*, 2017). After solvent evaporation samples were dissolved in 50 µl tetrahydrofuran : methanol : water $(4:4:1,$ v/v/v) for UPLC-nanoESI-MS/MS analysis.

Microsome preparation

For enhanced detection of GIPC and steryl glycoside (SG) species, microsomal fractions were prepared according to Abas & Luschnig (2010) from the collected protonemal tissue. The microsomal pellet was dissolved in water and lipids were extracted according to lipid extraction described previously.

Sphingolipid and SG analysis

Measurement of targeted molecular sphingolipid and SG species was performed using the multiple reaction monitoring (MRM)-based UPLC-nanoESI-MS/MS approach as described (Resemann *et al.*, 2021). LCB-Ps were measured in negative ionisation mode with $[M-H]^-$ as precursor ions. The more complex GIPC classes containing *N*-acetylhexosamine (HexNAc) and glucuronic acid (GlcA) HexNAc-GlcA-IPCs and Hex-HexNAc-GlcA-IPCs were measured in positive ionisation mode with $[M + NH_4]^+$ as precursor ions and ceramide fragments as product ions. Head group-specific ions were detected as described (Buré *et al.*, 2011). The following standards were used for sphingolipid quantification: LCB (d17:0), LCB-P (d17:1), Cer (d18:1/c12:0), for GlcCers and GIPCs: GlcCer (d18:1/c12:0). LC-MS data were processed using ANALYST 1.6.2 and MULTIQUANT 3.0.2 software (both AB Sciex). Absolute and relative peak areas are listed in Tables S6–S11.

Confocal laser scanning microscopy (CLSM)

Callose labelling followed Schuette *et al.* (2009); 1- to 2-wk-old protonemata were de-stained overnight in ethanol : acetic acid (3 : 1, v/v), then incubated in 0.1% (w/v) aniline blue in 50 mM sodium phosphate buffer (pH 9) for 30 min at room temperature and rinsed in buffer before visualisation. Images were captured using an excitation wavelength at 405 nm and an emission wavelength at 500 nm. Images were captured with Leica TCS SP5 confocal microscope (Leica Microsystems GmbH, Wetzlar, Germany) and processed using IMAGEJ 1.52b software (Schneider *et al.*, 2012). Images for subcellular localisation of *Pp*S4H were recorded using a Zeiss LSM 980 confocal microscope (Carl Zeiss Inc., Jena, Germany) with a ×40 objective. Cerulean was excited at 405 nm and detected at a wavelength of 436–495 nm; eYFP was excited at 514 nm and detected at a wavelength of 517–560 nm; chlorophyll was excited at 514 nm and detected at a wavelength of 646–690 nm.

Webtools

Sphinganine C-4 hydroxylases were searched using BLAST for *A. thaliana* SBH1 and SBH2 in the NCBI proteome database (National Center for Biotechnology Information (NCBI), US National Library of Medicine, MD, USA) (http://www.ncbi.nlm.nih.gov/BLAST/) for *P. patens* (Altschul *et al.*, 1990). S4H was assigned to 'Fatty acid hydroxylase superfamily' using the CDD database (Marchler-Bauer *et al.*, 2015; Lu *et al.*, 2020). Membrane protein topology was predicted using TMHMM

software (Sonnhammer *et al.*, 1998; Krogh *et al.*, 2001). Gene expression information was obtained using the *P. patens* eFP browser at: https://www.bar.utoronto.ca (Winter *et al.*, 2007; Ortiz-Ramírez *et al.*, 2016).

Results

## *Pp*S4H is a putative LCB C-4 hydroxylase in *P. patens* that localises to the ER

In *A. thaliana*, LCB C-4 hydroxylation is catalysed by two redundant LCB C-4 hydroxylases SBH1 and SBH2 (Sperling *et al.*, 2001; Chen *et al.*, 2008). BLAST searches using both proteins retrieved a single putative LCB C-4 hydroxylase in the *P. patens* proteome that had 68% and 63% identity to SBH1 and SBH2, respectively. The *P. patens* protein is 256 amino acids in length and is annotated in the NCBI database as sphinganine C4-monooxygenase 1-like (XP_024362887.1). Here, the protein is designated as sphinganine C-4 hydroxylase (S4H). Microarray data from the eFP browser revealed strong expression of *S4H* in all organs (Fig. S1a). The highest expression was detected in protonemata, gametophores and mature spore capsules. The constitutive expression pattern resembled that of *SBH1* and *SBH2* in *A. thaliana*, and suggested an important role for S4H in all developmental stages of *P. patens*. Similar to other identified membrane-bound hydroxylases and desaturases, S4H contains three characteristic histidine motifs within its hydroxylase domain that are thought to be responsible for coordinating the di-iron cluster in the active site (Shanklin & Cahoon, 1998; Bai *et al.*, 2015) (Fig. S1b,c). S4H also contains two transmembrane domains as predicted by the TMHMM web tool (Fig. S1d). Most identified plant sphingolipid enzymes are located in the ER membrane (Luttgeharm *et al.*, 2016), including *A. thaliana* SBH1 and SBH2 (Chen *et al.*, 2008). To confirm subcellular localisation of the *P. patens* LCB hydroxylase S4H to the ER, 10-d-old *P. patens* protonemata were bombarded with gold particles covered with plasmids carrying *PpS4H* and the ER marker KDEL (Mueller & Reski, 2015). The C-terminally eYFP-tagged *Pp*S4H showed colocalisation to the cerulean-tagged ER marker KDEL (Fig. 2a, b). Two planes of the same protonema cell showed *Pp*S4H and KDEL localisation in (a) an ER network pattern and (b) at the nuclear envelope.

*Pp*S4H restores trihydroxy LCB formation in *S. cerevisiae* LCB C-4 hydroxylase knockout mutant *sur2Δ*

To confirm the annotated LCB C-4 hydroxylase function of S4H, its coding sequence was codon usage optimised for *S. cerevisiae* expression. The optimised gene was expressed in the LCB C-4 hydroxylase *S. cerevisiae* knockout mutant *sur2Δ*. *sur2Δ* lacks all trihydroxy LCBs but the yeast cells remain viable (Haak *et al.*, 1997). Expression of *P. patens* S4H in *sur2Δ* successfully restored the formation of trihydroxy LCBs in both the ceramide (Fig. 2c) and LCB pools (Fig. S2). Notably, plants usually exclusively contain C18 LCBs, while *S. cerevisiae* contains both C18 and C20 LCBs. Both C18 and C20 LCBs were hydroxylated in
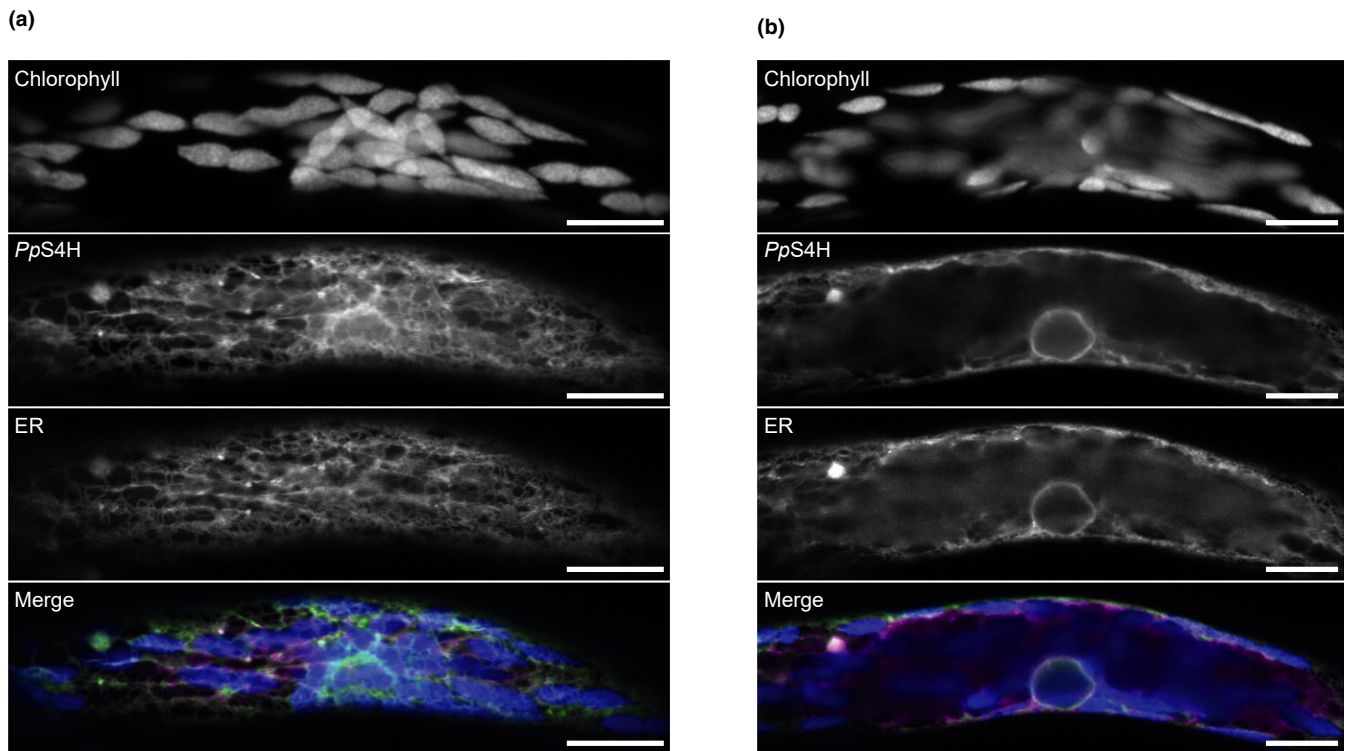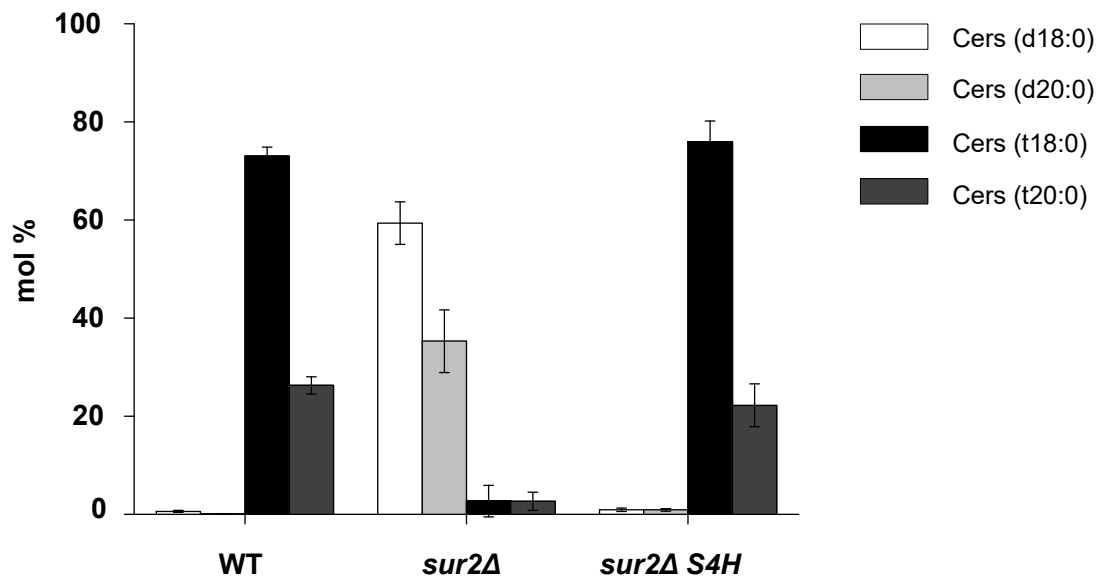
Fig. 2 *Physcomitrium patens* S4H colocalises with the endoplasmic reticulum (ER) marker KDEL in particle bombarded protonema cells. (a, b) Transient transformation of *P. patens* tissue with *Pp*S4H and KDEL was achieved through particle bombardment of 10-d-old protonema tissue. A transformed protonema cell is shown with chlorophyll autofluorescence (upper row), *Pp*S4H-eYFP fluorescence (second row), mCerulean-KDEL fluorescence (third row) and the merged image of all three channels (fourth row). Merged images show chlorophyll autofluorescence in blue, *Pp*S4H-eYFP fluorescence in green and mCerulean-KDEL fluorescence in magenta. Images of the same cell were taken at two different planes. (a) The first plane depicts colocalisation of the ER network and *Pp*S4H within the protonema cell. (b) The second plane depicts colocalisation of the ER and *Pp*S4H at the nuclear envelope. Bars, 10 μm. The experiment was performed once. Photographs are representative images for 21 transformed cells. (c) Complementation of *Saccharomyces cerevisiae* LCB C-4 hydroxylase knockout mutant *sur2Δ* with *P. patens* S4H restores the formation of trihydroxy LCB-containing ceramides. Ceramide profiles of *S. cerevisiae* wild-type (WT), *sur2Δ* knockout strain and *sur2Δ* knockout strain complemented with *P. patens* LCB C-4 hydroxylase S4H are shown. Ceramide species (Cers) with the same LCB moiety are summed up and are categorised into dihydroxy (d18:0, d20:0) or trihydroxy (t18:0, t20:0) ceramides with 18 or 20 LCB carbon chain lengths. Data represent the mean ± SD of four independent biological replicates.

S. cerevisiae by *P. patens* S4H. This finding confirmed the predicted enzymatic activity of S4H and showed that S4H activity was not highly specific for LCB carbon chain length.

Loss of trihydroxy LCBs reshapes sphingolipid metabolism in *P. patens*

Two independent loss-of-function *s4h* mutants (*s4h-1* and *s4h-2*) were generated by homologous recombination. In both lines, the *S4H* transcript was completely absent, as determined by reverse transcriptase PCR analysis (Fig. 3a). To study the *in vivo* effects of the complete loss of LCB C-4 hydroxylation on the sphingolipidome of *P. patens*, protonemata were cultured for 10 d on cellophane covered BCD medium. After lipid extraction, the sphingolipid profiles were determined using UPLC-nanoESI-MS/MS. Relative profiles and fold changes of absolute peak areas compared with the wild-type were analysed for LCBs, ceramides,

GlcCers and GIPCs. Sphingolipid classes showed varying detection efficiencies in different extraction fractions. GIPC content was measured in microsomes prepared from protonemata to enrich these membrane-bound sphingolipids; all other classes were analysed in crude protonema lipid extract. These different lipid preparations gave the best representations of changes in each sphingolipid class between *P. patens s4h* mutants and wild-type.

Wild-type t18:0 LCB accounted for 94% and d18:0 LCB for 6% of the total, however *s4h-1* and *s4h-2* had no t18:0 LCB and instead contained 99% d18:0 LCB (Fig. 3b). The mutants additionally contained minor amounts of d18:1 and d18:2 LCBs (0.5% and 0.1%, respectively). In the wild-type LCB-P profile t18:0 LCB-P also predominated with more than 60% of the total (Fig. 3c), d18:0 LCB-P accounted for *c.* 30%. In *s4h-1* and *s4h-2*, no t18:0 LCB-P was detected. Instead, over 99% was d18:0 LCB-P and *c.* 0.3% d18:1 LCB-P. d18:2 LCB-P was only detected in trace amounts in the *s4h* mutants. Overall, there was
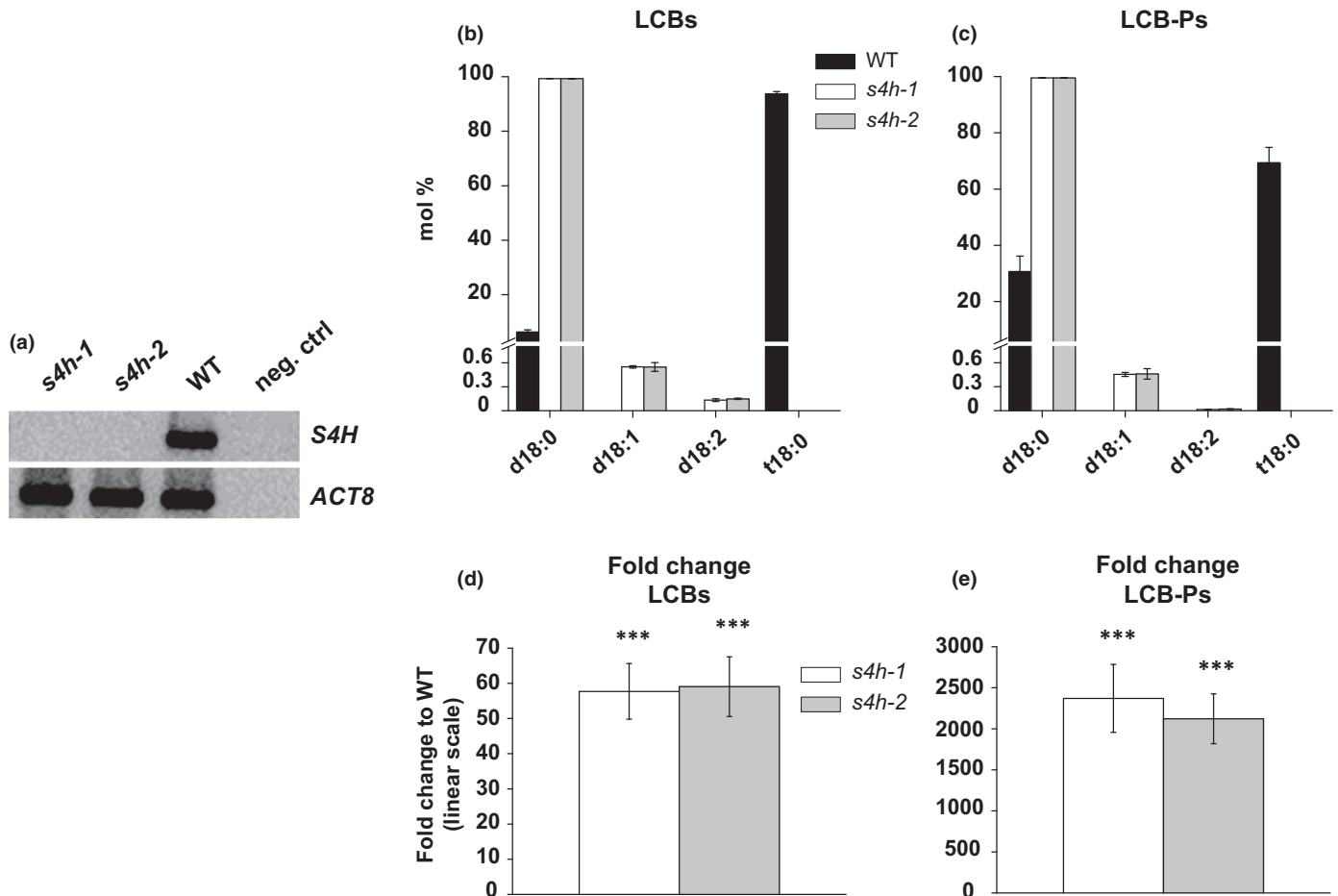
Fig. 3 *Physcomitrium patens s4h* mutant characterisation and altered long-chain base (LCB) content of *s4h-1* and *s4h-2*. (a) *S4H* transcript determination by reverse transcriptase PCR. *ACTIN8* (*ACT8*) was used as reference gene and water as a negative control (neg. ctrl). (b–e) Long-chain bases (LCBs) and phosphorylated LCBs (LCB-Ps) were extracted from protonemata of 10-d-old wild-type (WT), *s4h-1* and *s4h-2 P. patens* and analysed using UPLC-nanoESI-MS/MS. Dihydroxy LCBs are indicated by a 'd' and trihydroxy LCBs are indicated by a 't'. Relative profiles of (b) LCBs and (c) LCB-Ps in WT, *s4h-1* and *s4h-2* lines. Fold changes of (d) LCBs and (e) LCB-Ps compared with the WT were calculated using absolute peak areas. Fold changes are depicted in linear scale. The WT, which is not shown, was set to 1. Sphingolipid data represent the mean ± SD of measurements from four independent cultivations each containing protonema material from eight cultivation plates. Statistical analysis was performed using Student's *t*-test. Asterisks indicate significance levels at ***, *P* < 0.001 compared with the WT.

a >60-fold accumulation of LCBs and a >2000-fold accumulation of LCB-Ps in the *s4h* mutants compared with the wild-type (Fig. 3d,e).

The drastic increase in LCBs and LCB-Ps is consistent with findings from *A. thaliana sbh1 sbh2* (Chen *et al.*, 2008). As the absolute content of downstream sphingolipid classes was also affected in *sbh1 sbh2*, it was hypothesised that this might also be the case in *P. patens*. Surprisingly, there was no change in the total ceramide amount of the *s4h* mutants compared with the wild-type (Fig. S3b). In the wild-type, ceramides with the t18:0 LCB moiety predominated (Fig. 4a,d) while, in the *s4h* mutants, the most abundant LCB moiety was d18:0, with lesser amounts of d18:1 and d18:2 (Fig. 4b,c,e,f).

Ceramides were grouped according to the hydroxylation state of their fatty acids. By this categorisation, ceramides contain unhydroxylated fatty acids, indicated by a 'c' in front of the chain length number (Fig. 4a–c), and hydroxyceramides contain α-hydroxylated fatty acids, indicated by an 'h' in front of the chain length number (Fig. 4d–f). Relative ceramide and hydroxyceramide profiles revealed that the wild-type contained more hydroxyceramides, while the *s4h* mutants contained more ceramides (Fig. 4a–f). Fold change calculations confirmed this observation with *s4h-1* having 4.7-fold more and *s4h-2* having 4.4-fold more ceramides than the wild-type (Fig. 4g). Hydroxyceramides decreased in *s4h-1* to 40% and in *s4h-2* to 35% of the wild-type content. On a logarithmic scale, this corresponded to an increase in ceramide content in *s4h* mutants of *c.* 0.65 (Fig. 4g) and a reduction of hydroxyceramide content in *s4h* mutants of *c.* 0.42 (Fig. 4h).

The wild-type fatty acid profile of all ceramides was mainly composed of saturated fatty acids and a few unsaturated fatty acids ranging from C20 to C26 (Fig. 4a,d). Ceramides in *s4h-1* and *s4h-2* mutants showed a similar fatty acid profile with c16:0 emerging additionally in minor amounts (Fig. 4b,c,e,f).

Over 90% of the GlcCer profile of the wild-type was made up of a single molecular species, with a sphingoid backbone consisting of a d18:2 LCB moiety and a h20:0 fatty acid moiety (Fig. 5a). The predominant LCB moiety found in GlcCers of *s4h* mutants was also d18:2. The fatty acid profile of the *s4h* GlcCers was substantially broadened compared with the wild-type profile (Fig. 5b,c). The most abundant fatty acids in the mutants were saturated and unsaturated fatty acids ranging from C20 to C24 chain length. Total GlcCer levels were not significantly changed in *s4h* mutants compared with the wild-type control (Fig. S3c).

Over 90% of molecular species of *P. patens* wild-type GIPCs with one hexose (Hex) moiety attached to glucuronic acid (GlcA) linked inositolphosphorylceramide (IPC) had a t18:0 LCB moiety (Fig. 5d). Similar to changes in ceramide profiles, the predominant LCB moiety was changed from t18:0 to d18:0 in the *s4h* mutants. By contrast with the LCB moiety, the fatty acid composition of Hex-GlcA-IPCs was not changed in *s4h* mutants compared with the wild-type (Fig. 5d–f). The four most abundant fatty acids found in the Hex-GlcA-IPC pool were h20:0, h22:0, h24:0 and h24:1. Relative profiles were also determined for GIPCs with different polar head groups (Fig. S4). GIPCs may be grouped according to the complexity of their head group

composition. Series A GIPCs contain one additional sugar residue, Hex-GlcA-IPCs, which may also be in the form of *N*-acetylhexosamine (HexNAc), HexNAc-GlcA-IPCs. Series B GIPCs contain two additional sugar residues, Hex-Hex- and Hex-HexNAc-GlcA-IPCs. Series A and B are the main GIPCs described in *P. patens* (Cacas *et al.*, 2013) and were therefore used as representative GIPC analysis for *s4h* mutant characterisation in this study. The relative profiles of these complex GIPCs in the wild-type and in the *s4h* lines were similar to the described Hex-GlcA-IPC profiles (Fig. S4). Interestingly, fold change calculations using the absolute peak area given in counts per second (cps) revealed a slight increase (*c.* 1- to 2-fold) of series A GIPCs and a significant accumulation (*c.* 6-fold) of series B GIPCs in *s4h* lines compared with the wild-type (Fig. S5).

Analogous to ceramides, molecular species of GlcCers and Hex-GlcA-IPCs were sorted according to the hydroxylation status of their fatty acid moieties. Again, an increase in species with unhydroxylated fatty acids and a decrease in species with hydroxylated fatty acids was observed in the *s4h* lines (Fig. S6). Sphingolipid quantification in microsomal fractions confirmed the compositional changes in the sphingolipidome of *s4h* mutants compared to the wild-type (Tables S10, S11).

Taken together, these results showed that loss of LCB C-4 hydroxylation in *P. patens* caused a substantial shift in the composition of all sphingolipid classes. The most obvious changes were observed in the LCBs/LCB-Ps and LCB moieties of ceramides and GIPCs, and in the fatty acid moieties of GlcCers. There was a substantial increase of LCBs as potential substrates of S4H. Except for significant accumulation of series B GIPCs, loss of LCB C-4 hydroxylation had no substantial effect on total content of downstream sphingolipid classes.

Loss of trihydroxy LCBs causes a change in the composition of conjugated sterols

Several studies on PM organisation have demonstrated a strong interaction network between different free and conjugated phytosterols and sphingolipids (Grosjean *et al.*, 2015; Grosjean *et al.*, 2018). A result of these interactions is the formation of microdomains and nanodomains, which are considered to be important sorting platforms for membrane proteins (Simons & Ikonen, 1997; Cacas *et al.*, 2012). Connections between sterols and sphingolipids are mediated by hydrogen bonding (Slotte, 1999; Slotte, 2016; Mamode Cassim *et al.*, 2019). The change of the hydroxylation pattern of sphingoid backbones in the *s4h* mutants might, therefore, potentially also influence interactions between sterols and sphingolipids in the PM and, perhaps by extension, sterol content. To test this hypothesis, the relative profile of SGs was analysed in microsomes obtained from protonemata of wild-type and *s4h* plants (Fig. 6). At 47% of the total, campesteryl represented the most abundant steryl moiety of SGs in the wild-type, followed by isofucosteryl (27%), sitosteryl (15%), stigmasteryl (9%) and brassicasteryl (2%). Cholesteryl was only detected in trace amounts (0.07%). While the general SG profile and total SG content were maintained in *s4h* mutants, a significant increase compared with the wild-type was observed
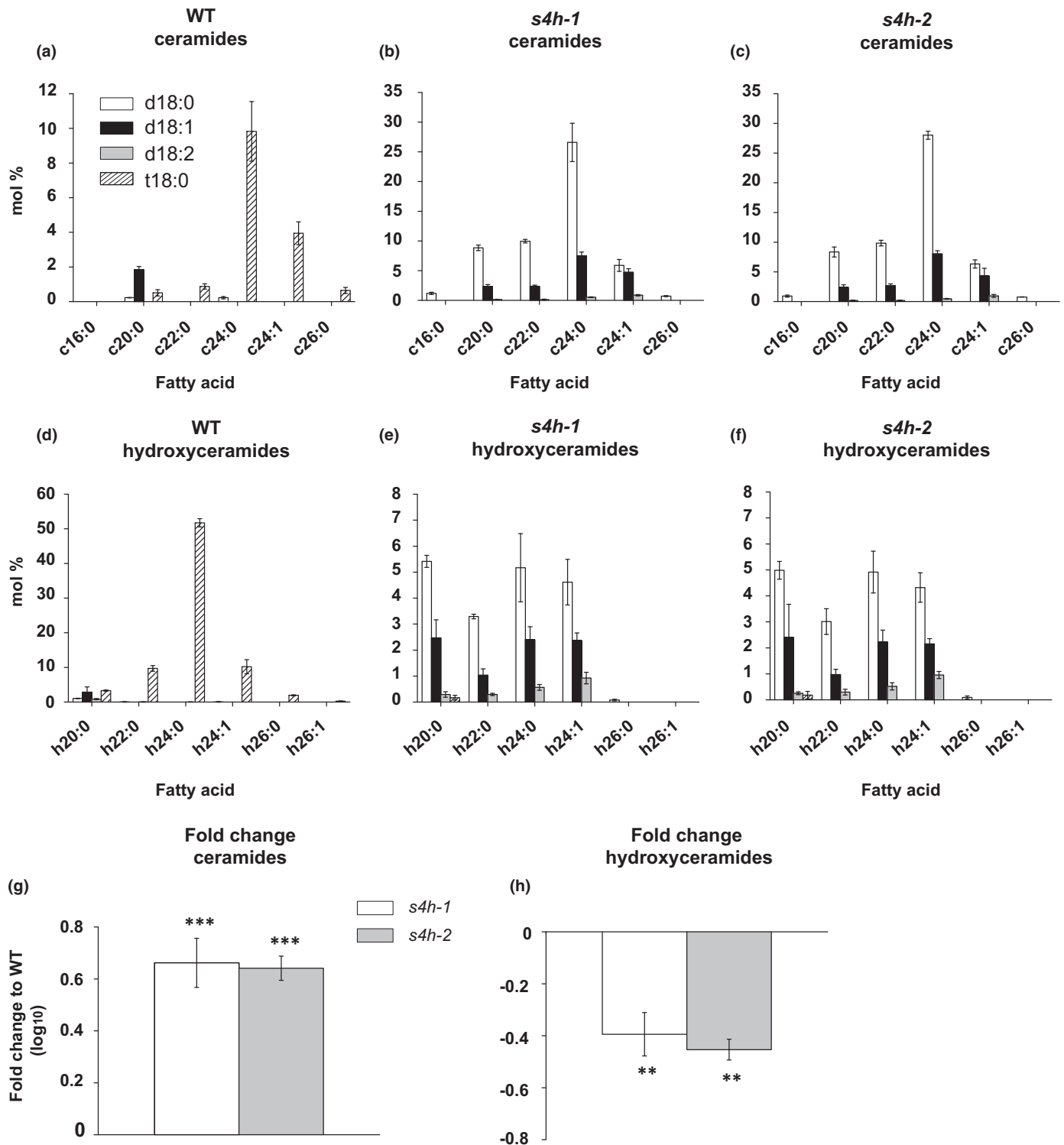
Fig. 4 *Physcomitrium patens s4h-1* and *s4h-2* have an altered ceramide content. (a–h) Ceramides were extracted from protonemata of 10-d-old wild-type (WT), *s4h-1* and *s4h-2 P. patens* and analysed using UPLC-nanoESI-MS/MS. Relative profiles of (a–c) ceramide and (d–f) hydroxyceramide molecular species are shown with their long-chain base (LCB) (column colour) and fatty acid (*x*-axis) moieties. Dihydroxy LCB moieties are indicated by a 'd' and trihydroxy LCB moieties are indicated by a 't'. Molecular species with an unhydroxylated fatty acid moiety are indicated by a 'c' and molecular species with an α-hydroxylated fatty acid moiety are indicated by an 'h'. Relative profiles of (a) WT, (b) *s4h-1* and (c) *s4h-2* ceramides with unhydroxylated fatty acid moieties. Relative profiles of (d) WT, (e) *s4h-1* and (f) *s4h-2* hydroxyceramides with α-hydroxylated fatty acid moieties. (g) Ceramide and (h) hydroxyceramide fold changes compared with the WT were calculated using absolute peak areas and are depicted in log₁₀ scale. The WT, which is not shown, was set to 0. Sphingolipid data represent the mean ± SD of measurements from four independent cultivations each containing protonema material from eight cultivation plates. Statistical analysis was carried out using Student's *t*-test. Asterisks indicate different significance levels at ***, $P < 0.001$ and **, $P < 0.01$ compared with the WT.
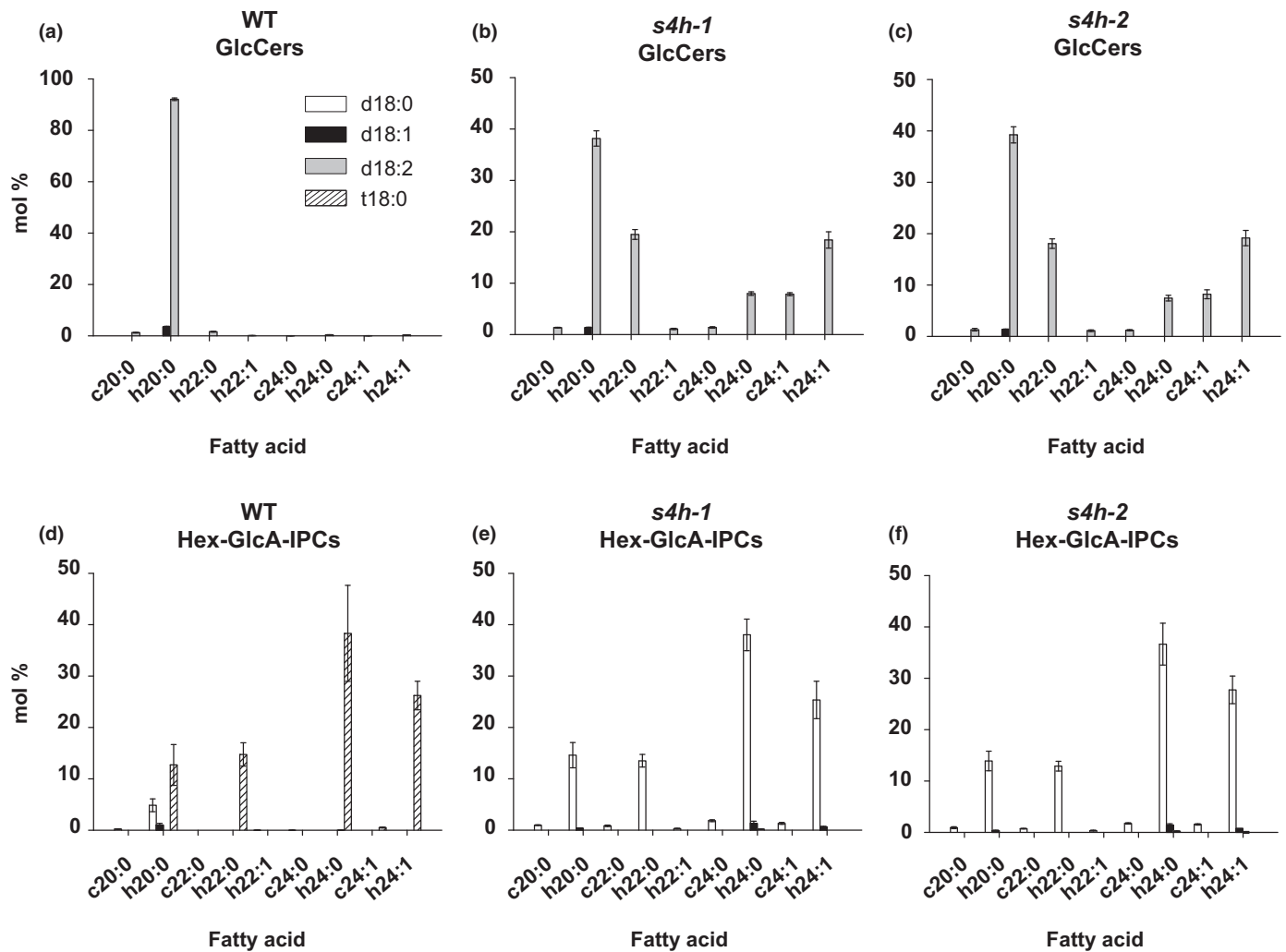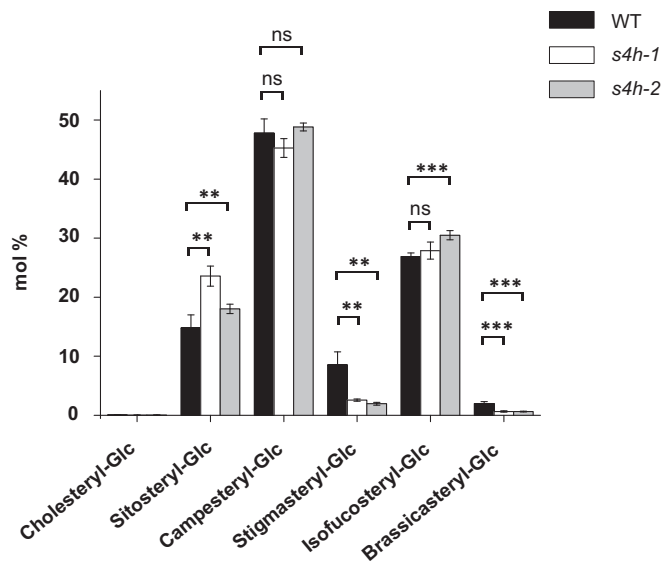
Fig. 5 *Physcomitrium patens s4h-1* and *s4h-2* have altered glycosylceramides (GlcCer) and glycosyl inositolphosphorylceramides (GIPC) profiles. (a–c) GlcCers were extracted from protonemata of 10-d-old wild-type (WT), *s4h-1* and *s4h-2 P. patens*. (d–f) GIPCs were extracted from microsomes prepared from protonemata of 10-d-old WT, *s4h-1* and *s4h-2 P. patens*. Sphingolipids were analysed using UPLC-nanoESI-MS/MS. GlcCer and Hex-GlcA-IPC molecular species are shown with their long-chain base (LCB) (column colour) and fatty acid (x-axis) moieties. Dihydroxy LCB moieties are indicated by a 'd' and trihydroxy LCB moieties are indicated by a 't'. Molecular species with an unhydroxylated fatty acid moiety are indicated by a 'c' and molecular species with an α-hydroxylated fatty acid moiety are indicated by an 'h'. (a–c) Relative GlcCer profiles of (a) WT, (b) *s4h-1* and (c) *s4h-2*. Only molecular species with a peak area ≥ 1% in at least one of the three lines were included in the GlcCer graphs. (d–f) Relative Hex-GlcA-IPC profiles of (d) WT, (e) *s4h-1* and (f) *s4h-2*. Only molecular species with a peak area ≥ 0.5% in at least one of the three lines were included in the Hex-GlcA-IPC graphs. Sphingolipid data represent the mean ± SD of measurements from four independent cultivations each containing protonema material from eight cultivation plates. GlcA, glucuronic acid; Hex, hexose; IPCs, inositolphosphorylceramides.

for sitosteryl and isofucosteryl (Fig. S7). A significant decrease was observed for stigmasteryl and brassicasteryl.

s4h mutants show impaired growth and development in all tissues

The observed changes in sphingolipid and sterol composition suggest a change in membrane organisation that could affect cell growth and division. Furthermore, the *A. thaliana* double knock-out mutant *sbh1 sbh2* showed defects in cell elongation and division, causing severely dwarfed plants that failed to reach reproductive maturity (Chen *et al.*, 2008). Gametophyte

development of the *P. patens s4h* mutants was studied to determine whether they were similarly affected. Protonema spot inocula of *c.* 1 mm in diameter were placed on BCD medium. After 12 d of growth the wild-type plant developed a star-shaped colony with long, branched protonemal filaments (Fig. 7a). Small gametophores developed in the centre of the colony. *s4h* mutants also developed protonemal filaments, however colonies had a rounded, less branched appearance than the wild-type. No gametophores could be observed emerging from the centre of the colony. After 24 d of growth, the wild-type showed fully developed gametophores that completely overgrew the protonemal tissue. *s4h* mutants showed no gametophore development and

Fig. 6 *Physcomitrium patens s4h-1* and *s4h-2* have altered steryl glycoside (SG) profiles. SGs were extracted from microsomes prepared from protonemata of 10-d-old wild-type (WT), *s4h-1* and *s4h-2 P. patens* and analysed with UPLC-nanoESI-MS/MS. Relative SG profiles of WT, *s4h-1* and *s4h-2*. SG data represent the mean ± SD of measurements from four independent cultivations each containing protonema material from eight cultivation plates. Statistical analysis was carried out using Student's *t*-test. Asterisks indicate different significance levels at ***, $P < 0.001$; **, $P < 0.01$; and not significant (ns) at $P > 0.05$ compared with the WT. Glc: glycoside.

protonemal filaments remained stunted. After 37 d of growth, severely dwarfed gametophores were finally observed in *s4h* colonies, with diameters of *c.* 0.4 mm.

Protonema consists of two cell types: chloroplast-rich chloronema cells and caulonema cells that contain fewer and less well developed chloroplasts. Regarding *s4h* colony growth, it was speculated that the transition from chloronema to caulonema cells might be impaired. To have a more extensive look at protonema differentiation, a dark growth experiment was performed. Protonema spot inocula of the wild-type, *s4h-1* and *s4h-2* lines were placed on BCDAT medium supplemented with 2% sucrose. After growth for 1 wk under continuous light the wild-type and *s4h* mutant colonies looked alike (Fig. 7b). Colonies developed a dense green centre consisting of filamentous protonema cells. Subsequently, plates were transferred to the dark and put into vertical orientation. Cultivation under these conditions was continued for 3 wk. The developing filamentous cells in the wild-type did not contain chloroplasts and had a brownish appearance. The developed cells are a subtype of caulonema, specified as skotonema. Wild-type skotonema cells formed numerous long filaments reaching upwards. Although *s4h* mutants were able to generate skotonema cells, their filaments were much shorter, fewer and had an altered morphology compared with wild-type cells. Gametophytic development, including both gametophore and protonemal tissues, was therefore drastically impaired in *s4h* mutants.

To quantify the growth defect of *s4h* mutants, protonemata were cultured on cellophane-covered BCD medium plates. Each

plate was inoculated with a protonemal cell suspension that was adjusted to a volume corresponding to 5 mg DW. Protonemal tissue was maintained on plates for 10 d before harvesting and determination of FW. In four independent experiments, wild-type tissue reached a mean biomass of *c.* 4.4 g (Fig. 7c), while *s4h* mutants generated significantly less biomass, *c.* 2.3 g. Determination of the DW confirmed this effect (Fig. S8).

Imbalance of sphingolipid metabolism alters callose deposition at protonema cross-walls

P. patens s4h mutants have severe growth defects, similar to *A. thaliana* sphingolipid mutants (Chen *et al.*, 2008). In *A. thaliana sbh1 sbh2* these growth defects were attributed to impaired cell elongation and division (Chen *et al.*, 2008). Another study showed that inhibition of VLCFA sphingolipid synthesis caused abnormal cell plate formation in root tips (Molino *et al.*, 2014). Defects in cell plate formation are believed to arise from impaired vesicle and membrane trafficking, affecting the deposition of cell wall material during cell division. Callose is a cell wall component deposited during plant cytokinesis; in *P. patens* protonemata, callose is deposited during cell division at the cross-walls separating two filamentous cells (Scherp *et al.*, 2001; de Keijzer *et al.*, 2017). To determine whether *s4h* mutants also have abnormal cell plate formation, callose was stained in 1- to 2-wk-old protonema tissue using aniline blue and imaged using CLSM. In wild-type protonema cells callose was exclusively found in the cross-walls between two filamentous cells, in a clear line without irregularities (Fig. 8). Cross-walls in *s4h* mutants, however, were abnormally shaped. Callose was still deposited at cross-walls but irregular stretches could be seen on both sides of the wall. These were perpendicular to the cross-wall and extended towards the centre of adjacent filamentous cells. The vast majority of *s4h* protonema cells showed cross-wall malformations of different degrees.

Discussion

Sphingolipids containing trihydroxy LCB moieties predominate in plants (Markham *et al.*, 2006). A study of *A. thaliana sbh* mutants revealed that trihydroxy sphingolipids are crucial for plant growth and development (Chen *et al.*, 2008). To examine the role of trihydroxy sphingolipids in nonvascular plants, the LCB C-4 hydroxylase S4H from *P. patens* was characterised. The enzyme was identified based on sequence homology and its metabolic activity was confirmed by complementation of the *S. cerevisiae sur2Δ* mutant. Sphingolipid analysis of *s4h* null mutants revealed complete depletion of trihydroxy sphingolipids, and substantial enrichment of LCB substrates. Consistent with *sbh1 sbh2* in *A. thaliana*, *s4h* plants were impaired in growth and development. The developmental phenotype was accompanied by irregular callose depositions at the cross-walls of filamentous *s4h* protonema cells.

Loss of all t18:0 LCB-containing sphingolipids in *s4h* mutants confirmed that the LCB C-4 hydroxylase is encoded by a single gene in *P. patens*. As in *A. thaliana sbh1 sbh2*, loss of the
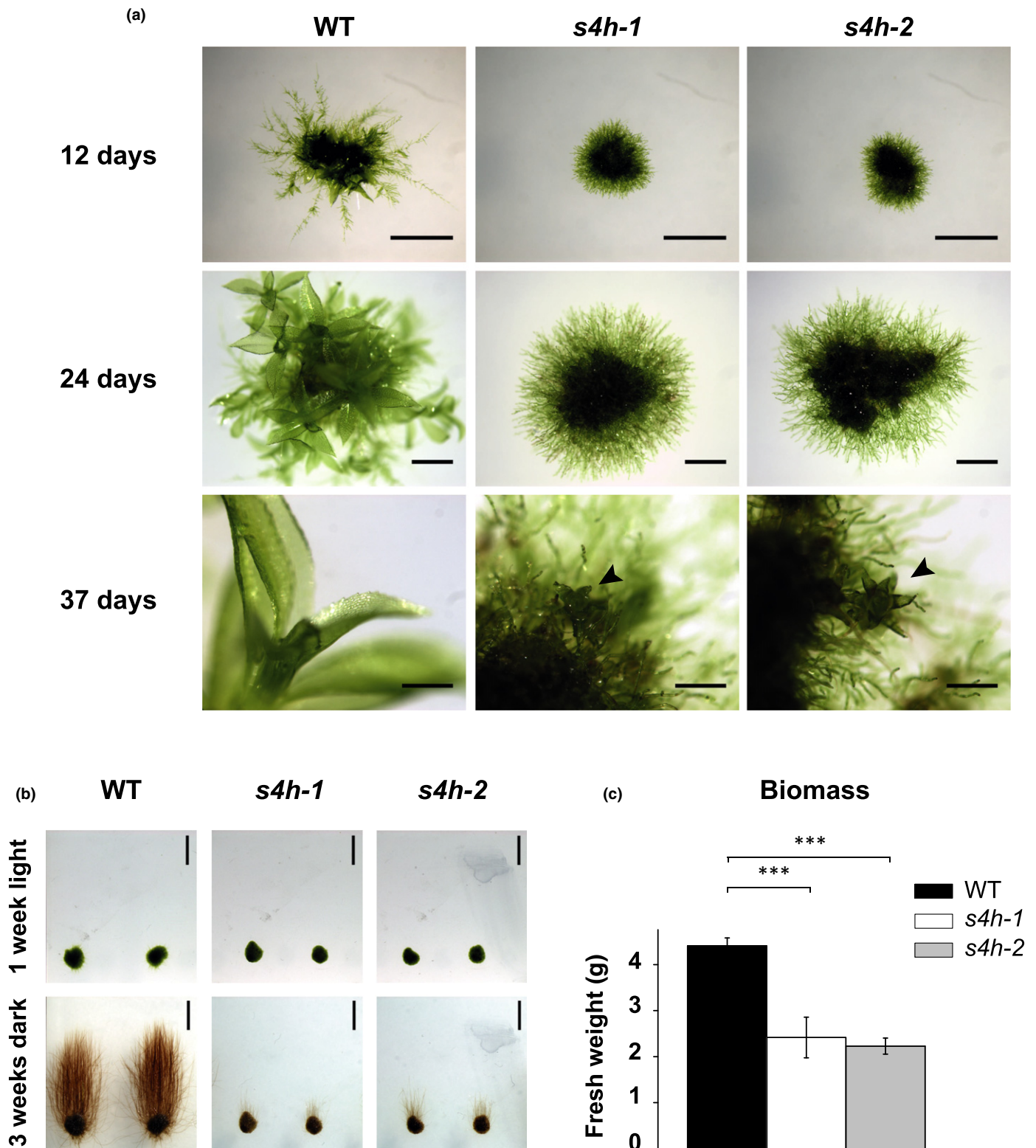
Fig. 7 *Physcomitrium patens s4h-1* and *s4h-2* lines show a growth phenotype in all gametophytic stages. (a) 1 mm protonema spot inocula of wild-type (WT), *s4h-1* and *s4h-2* were placed on BCD medium and grown for the indicated time periods. Bars in 12-d colony images, 4 mm. Bars in 24-d colony pictures, 1 mm. Bars in 37-d colony pictures, 0.4 mm. Arrowheads indicate gametophores on *s4h-1* and *s4h-2* colonies. (b) Spot inocula of *P. patens* WT, *s4h-1* and *s4h-2* were placed on BCDAT + 2% sucrose and grown under continuous light for 1 wk (upper row). Plates were moved to the dark and rotated into a vertical position. Colonies were grown for another 3 wk to induce skotonema development (lower row). Bars, 0.5 cm. (c) Growth of WT, *s4h-1* and *s4h-2* was quantified by collecting 10-d-old protonema tissue grown on cellophane-covered BCD medium and determining the FW. Data represent the mean ± SD of measurements from four independent cultures, each containing protonema material from eight cultivation plates. Statistical analysis was carried out using Student's *t*-test. Asterisks indicate significance level at ***, $P < 0.001$ compared with the WT.

WT   *s4h-1*   *s4h-2*
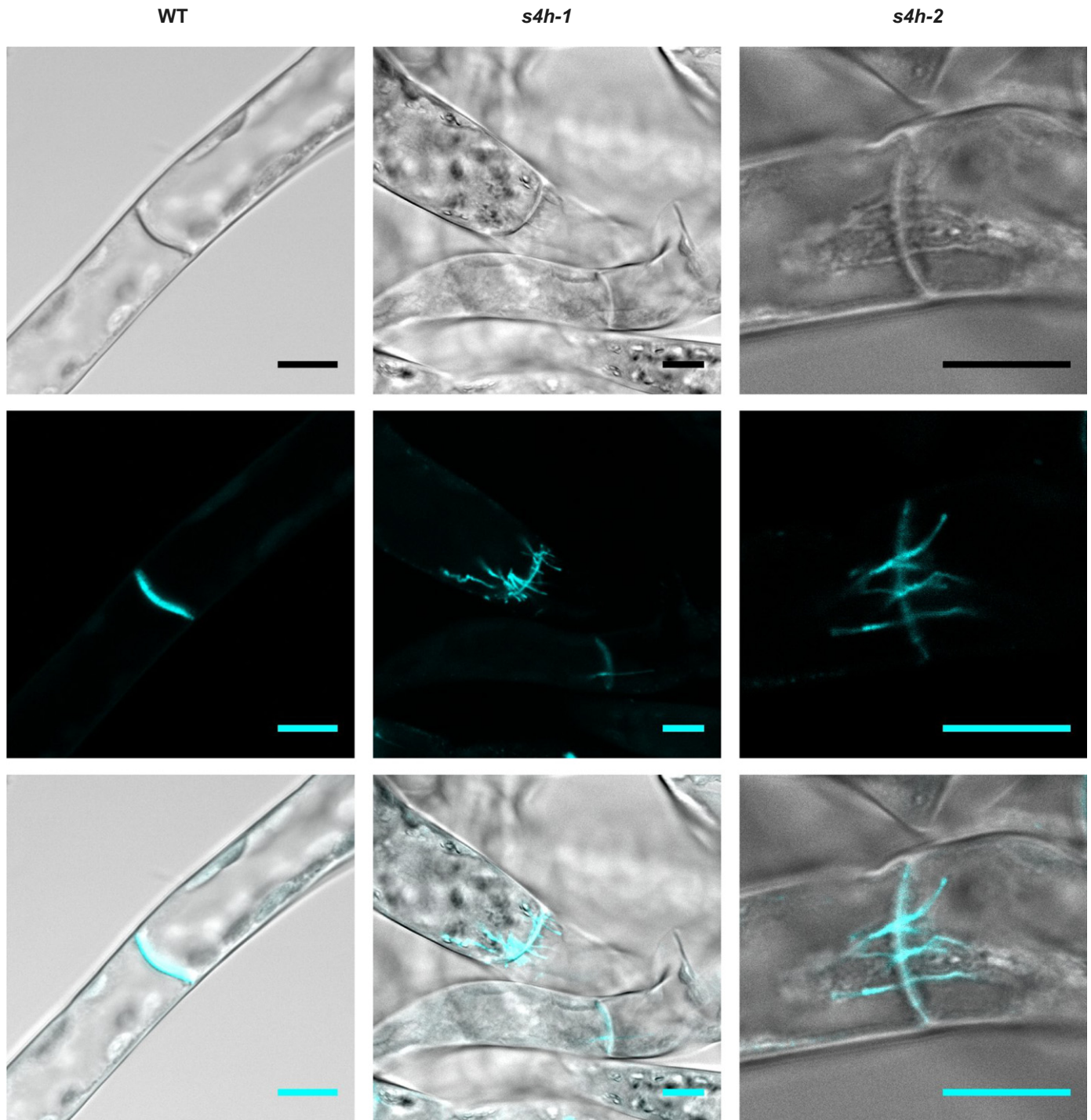
Fig. 8 Irregular callose deposition at cross-walls of *P. patens s4h-1* and *s4h-2* protonema cells. Cross-walls of 1- to 2-wk-old filamentous wild-type (WT), *s4h-1* and *s4h-2* protonema cells were captured using confocal laser scanning microscopy. Callose was stained with aniline blue. Photographs are shown in bright field (top row), in aniline blue fluorescence (middle row) and as the merged image of both (bottom row). Bars, 10 μm. Photographs are representative of three independent experiments.

trihydroxy LCB moiety in *s4h* caused a shift of the most abundant species from trihydroxy towards dihydroxy LCB moieties. The shift was observed in *P. patens* for LCBs, ceramides and GIPCs, but not for GlcCer, as the wild-type GlcCer pool only contains d18:2 LCBs but no t18:0 LCBs (Resemann *et al.*, 2021).

Loss of trihydroxy LCBs in *A. thaliana* was accompanied by a total increase of all sphingolipid classes (Chen *et al.*, 2008). In *P. patens* only LCBs, LCB-Ps and series B GIPCs were found to have substantially raised levels in *s4h* mutants compared with the wild-type. The total ceramide, GlcCer and series A GIPC content was only slightly or not significantly affected. *P. patens s4h* had a

much higher fold change for LCB-Ps (*c.* 2000-fold) than for LCBs (*c.* 60-fold) compared with the wild-type. Possibly, the excess of d18:0 LCBs exceeds the capacity of d18:0-specific ceramide synthases to incorporate all LCBs into ceramides. It is known from vascular plants that application of LCBs induces PCD (Shi *et al.*, 2007), while application of LCB-Ps suppresses PCD (Shi *et al.*, 2007; Alden *et al.*, 2011). The balance of LCBs and LCB-Ps is therefore considered an important factor in PCD induction (Shi *et al.*, 2007; Alden *et al.*, 2011). To dispose of excess LCBs in *P. patens s4h*, it could be that a large part is phosphorylated. The resulting higher levels of LCB-Ps might outweigh accumulation of LCBs and therefore suppress LCB-induced cell death. This idea is supported by the phenotype, as no cell death was observed in *s4h* mutants. However, studies concerning LCB kinase and phosphatase activity, as well as the contribution of LCBs and LCB-Ps on PCD induction, are still lacking in *P. patens* and need to be addressed in the future.

A. thaliana sbh1 sbh2 accumulated sphingolipids with C16 fatty acids, prompting speculation that this was responsible for the mutant's growth defect (Chen *et al.*, 2008). In the *P. patens* sphingolipidome, C16 fatty acids only represent a minor fatty acid moiety, which was not enriched in *s4h* mutants. Therefore, it appears unlikely that the growth phenotype observed in *A. thaliana* and *P. patens* resulted from accumulation of LCFAs in sphingolipids.

Physcomitrium patens s4h-1 and *s4h-2* accumulated ceramides, Hex-GlcA-IPCs and GlcCers with unhydroxylated fatty acids. While this was not observed for *A. thaliana sbh1 sbh2*, it has been described for *S. cerevisiae sur2Δ* cells (Haak *et al.*, 1997). This finding indicates that fatty acid hydroxylase might prefer ceramides containing trihydroxy LCBs as substrates. Indeed, the *A. thaliana* fatty acid hydroxylase mutant *fah1 fah2* had raised levels of sphingolipids with trihydroxy LCB moieties, indicating that these compounds are the favoured substrates of fatty acid hydroxylases (König *et al.*, 2012). Fatty acid hydroxylases have yet to be characterised in *P. patens*.

The fatty acid profiles in the complex sphingolipids GlcCers and GIPCs indicated that enzymes adding different head groups to the ceramide backbone have preferences for specific LCB modifications. While *P. patens* homologues for inositolphosphorylceramide synthases prefer ceramides with a t18:0 LCB moiety, the glycosylceramide synthase homologue works on ceramides with a d18:2 LCB moiety. Additionally, series B GIPCs (Hex-HexNAc-GlcA-IPCs) accumulated more strongly in *s4h-1* and *s4h-2* than series A GIPCs (HexNAc-GlcA-IPCs). As detection of GIPC classes with more complex head groups is a recent achievement (Buré *et al.*, 2011; Cacas *et al.*, 2013), it is not known whether GIPC classes in *A. thaliana sbh1 sbh2* were also differently affected.

LCB C-4 hydroxylases are functionally related to sphingolipid Δ4-desaturases. In mammals, LCB C-4 hydroxylase and sphingolipid Δ4-desaturase activities are carried out by a bifunctional enzyme, designated DES2 (Sperling *et al.*, 2001; Mizutani *et al.*, 2004). In *A. thaliana*, sphingolipid Δ4-desaturase is only expressed in flowers, while analysis is usually carried out on vegetative tissues. It was therefore difficult to exclude the possibility

that the *A. thaliana* sphingolipid Δ4-desaturase also produces hydroxylated LCBs (Chen *et al.*, 2008). The authors speculated that sphingolipid Δ4-desaturase might show a more prominent hydroxylase activity in phyla containing high amounts of Δ4-unsaturated LCBs, such as Solanaceae (Dunn *et al.*, 2004; Sperling *et al.*, 2005; Markham *et al.*, 2006; Markham & Jaworski, 2007). In these plants, the Δ4-desaturase may be ubiquitously expressed and could contribute either or both hydroxylase/desaturase functions in different tissues. The *P. patens* sphingolipidome more closely resembles that of Solanaceae than that of Brassicaceae, with d18:2 LCB being the only LCB moiety identified in the GlcCer pool (Markham *et al.*, 2006; Resemann *et al.*, 2021). This finding hints at high sphingolipid Δ4-desaturase activity in *P. patens*. As the knockout of S4H in *P. patens* resulted in loss of all detectable trihydroxy LCBs, this indicates that S4H is likely to account for all trihydroxy LCB synthesis. Sphingolipid Δ4-desaturase probably does not contribute to LCB hydroxylation in *P. patens*.

Cumulative findings from both *A. thaliana* and *P. patens* showed that defects in growth and development may be caused by the shift from trihydroxy to dihydroxy LCB moieties and the accompanied biophysical changes in the membrane. Changes in the SG composition in *P. patens s4h* mutants is evidence of this. Free phytosterols and their conjugated forms, SGs and acylated SGs (ASGs), were shown to induce microdomain formation (Grosjean *et al.*, 2015, 2018). These domains are enriched in sterols and hydroxylated sphingolipids, mainly GIPCs (Cacas *et al.*, 2016). Microdomains are thought to be formed and maintained, in part, through an intermolecular hydrogen bond network (Slotte, 1999; Mombelli *et al.*, 2003; Slotte, 2016). Loss of one hydroxyl group in the sphingoid backbone of GIPCs may not only reduce the strength of the hydrogen bond network between sterols and sphingolipids but, as shown here, may also change the membrane lipid composition. Effects on microdomain formation might hamper protein sorting downstream and therefore influence developmental processes.

Altered membrane composition would explain the observed impaired callose deposition in *s4h* mutants. Callose is a cell wall component that is deposited at the cell plate during cytokinesis (Scherp *et al.*, 2001). Several mutations that affect GIPC structure (head group, trihydroxy LCB moiety, α-hydroxylated VLCFA moiety) cause developmental phenotypes in *A. thaliana* (Chen *et al.*, 2008; Bach *et al.*, 2011; Markham *et al.*, 2011; König *et al.*, 2012; Molino *et al.*, 2014). Molino *et al.*, (2014) observed malformed cell plates in root tip cells in which synthesis of VLCFA-containing sphingolipids, mainly GIPCs, was inhibited by fumonisin B1. Cell plates were either incomplete or were tilted, and their change was explained by defects in membrane fusion and vesicle trafficking. In *P. patens s4h* protonema cells, the cross-walls resulting from cytokinesis still appeared to be formed normally, however stretches of callose were observed trailing into the centre of adjacent cells. The stretches resembled the microtubule network, which is responsible for transporting vesicles loaded with wall material towards the cell plate during cytokinesis. This phenotype suggested disturbed vesicle

trafficking during cell division. The altered callose deposition at newly formed cross-walls in *P. patens* is a valuable indicator of the involvement of trihydroxy LCB-containing sphingolipids in cell division.

Callose deposition regulates the size exclusion limit of plasmodesmata (Vatén *et al.*, 2011). Plasmodesmata are symplastic channels that traverse the cell wall between adjacent cells and enable intercellular transport (Gallagher *et al.*, 2014; Tilsner *et al.*, 2016). The plasmodesmal PM is enriched in sterols and sphingolipids, the same lipids found in detergent-insoluble microdomains (Grison *et al.*, 2015; Liu *et al.*, 2020). Callose deposition is regulated by biosynthesis and degradation enzymes, which were found to be glycosylphosphatidylinositol (GPI)-anchored proteins (Simpson *et al.*, 2009; Zavaliev *et al.*, 2011). Impaired sterol biosynthesis affects the localisation of callose metabolic enzymes, causing abnormal callose accumulation and thereby limiting plasmodesmal transport (Grison *et al.*, 2015). Recent studies have confirmed that disruption of sphingolipid metabolism also alters callose deposition in response to *Botrytis cinerea* infection and at plasmodesmal sites (Bi *et al.*, 2014; Grison *et al.*, 2015; Liu *et al.*, 2020). Whether callose dislocation in *P. patens s4h* influences plasmodesmal function could be targeted in future studies to better understand the relationship between sphingolipids, callose and plasmodesmal function.

In summary, LCB hydroxylation has an important role in maintaining sphingolipid homeostasis in vascular and nonvascular plants, and loss of trihydroxy sphingolipids causes substantial growth defects. *P. patens* offers a valuable platform to study physiological and biochemical processes in complex and highly dynamic biological membranes. Together with findings from vascular plants and simple model membrane systems, this may contribute to fully understanding the physiological and metabolic function of sphingolipids.

ORCID

Ivo Feussner https://orcid.org/0000-0002-9888-7003
Cornelia Herrfurth https://orcid.org/0000-0001-8255-3255
Tegan M. Haslam https://orcid.org/0000-0002-4849-7330
Till Ischebeck https://orcid.org/0000-0003-0737-3822
Agnieszka Zienkiewicz https://orcid.org/0000-0003-0799-0521

References

Abas L, Luschnig C. 2010. Maximum yields of microsomal-type membranes from small amounts of plant material without requiring ultracentrifugation. *Analytical Biochemistry* **401**: 217–227.

Alden KP, Dhondt-Cordelier S, McDonald KL, Reape TJ, Ng CKY, McCabe PF, Leaver CJ. 2011. Sphingolipid long chain base phosphates can regulate apoptotic-like programmed cell death in plants. *Biochemical and Biophysical Research Communications* **410**: 574–580.

de Almeida RF, Fedorov A, Prieto M. 2003. Sphingomyelin/phosphatidylcholine/cholesterol phase diagram: boundaries and composition of lipid rafts. *Biophysical Journal* **85**: 2406–2416.

Altschul SF, Gish W, Miller W, Myers EW, Lipman DJ. 1990. Basic local alignment search tool. *Journal of Molecular Biology* **215**: 403–410.

Ashton NW, Cove DJ. 1977. The isolation and preliminary characterisation of auxotrophic and analogue resistant mutants of the moss, *Physcomitrella patens*. *Molecular and General Genetics* **154**: 87–95.

Bach L, Gissot L, Marion J, Tellier F, Moreau P, Satiat-Jeunemaitre B, Palauqui J-C, Napier JA, Faure J-D. 2011. Very-long-chain fatty acids are required for cell plate formation during cytokinesis in *Arabidopsis thaliana*. *Journal of Cell Science* **124**: 3223–3234.

Bai Y, McCoy JG, Levin EJ, Sobrado P, Rajashankar KR, Fox BG, Zhou M. 2015. X-ray structure of a mammalian stearoyl-CoA desaturase. *Nature* **524**: 252–256.

Berdyshev EV, Gorshkova IA, Garcia JG, Natarajan V, Hubbard WC. 2005. Quantitative analysis of sphingoid base-1-phosphates as bisacetylated derivatives by liquid chromatography–tandem mass spectrometry. *Analytical Biochemistry* **339**: 129–136.

Bi F-C, Liu Z, Wu J-X, Liang H, Xi X-L, Fang C, Sun T-J, Yin J, Dai G-Y, Rong C et al. 2014. Loss of ceramide kinase in *Arabidopsis* impairs defenses and promotes ceramide accumulation and mitochondrial H_2O_2 bursts. *Plant Cell* **26**: 3449–3467.

Buré C, Cacas JL, Wang F, Gaudin K, Domergue F, Mongrand S, Schmitter JM. 2011. Fast screening of highly glycosylated plant sphingolipids by tandem mass spectrometry. *Rapid Communications in Mass Spectrometry* **25**: 3131–3145.

Cacas J-L, Bure C, Furt F, Maalouf J-P, Badoc A, Cluzet S, Schmitter J-M, Antajan E, Mongrand S. 2013. Biochemical survey of the polar head of plant glycosylinositolphosphoceramides unravels broad diversity. *Phytochemistry* **96**: 191–200.

Cacas J-L, Buré C, Grosjean K, Gerbeau-Pissot P, Lherminier J, Rombouts Y, Maes E, Bossard C, Gronnier J, Furt F et al. 2016. Revisiting plant plasma membrane lipids in tobacco: a focus on sphingolipids. *Plant Physiology* **170**: 367–384.

Cacas J-L, Furt F, Le Guédard M, Schmitter J-M, Buré C, Gerbeau-Pissot P, Moreau P, Bessoule J-J, Simon-Plas F, Mongrand S. 2012. Lipids of plant membrane rafts. *Progress in Lipid Research* 51: 272–299.

Chen M, Markham JE, Dietrich CR, Jaworski JG, Cahoon EB. 2008. Sphingolipid long-chain base hydroxylation is important for growth and regulation of sphingolipid content and composition in *Arabidopsis*. *Plant Cell* 20: 1862–1878.

Dunn TM, Lynch DV, Michaelson LV, Napier JA. 2004. A post-genomic approach to understanding sphingolipid metabolism in *Arabidopsis thaliana*. *Annals of Botany* 93: 483–497.

Gallagher KL, Sozzani R, Lee CM. 2014. Intercellular protein movement: deciphering the language of development. *Annual Review of Cell and Developmental Biology* 30: 207–233.

Gietz RD, Schiestl RH. 2007. High-efficiency yeast transformation using the LiAc/SS carrier DNA/PEG method. *Nature Protocols* 2: 31–34.

Gonzalez Solis A, Han G, Gan L, Liu Y, Markham JE, Cahoon RE, Dunn TM, Cahoon EB. 2020. Unregulated sphingolipid biosynthesis in gene-edited Arabidopsis *ORM* mutants results in nonviable seeds with strongly reduced oil content. *Plant Cell* 32: 2474–2490.

Grison MS, Brocard L, Fouillen L, Nicolas W, Wewer V, Dörmann P, Nacir H, Benitez-Alfonso Y, Claverol S, Germain V et al. 2015. Specific membrane lipid composition is important for plasmodesmata function in Arabidopsis. *Plant Cell* 27: 1228–1250.

Grosjean K, Der C, Robert F, Thomas D, Mongrand S, Simon-Plas F, Gerbeau-Pissot P. 2018. Interactions between lipids and proteins are critical for plasma membrane ordered domain organization in BY-2 cells. *Journal of Experimental Botany* 69: 3545–3557.

Grosjean K, Mongrand S, Beney L, Simon-Plas F, Gerbeau-Pissot P. 2015. Differential effect of plant lipids on membrane organization: SPECIFICITIES OF PHYTOSPHINGOLIPIDS AND PHYTOSTEROLS. *Journal of Biological Chemistry* 290: 5810–5825.

Haak D, Gable K, Beeler T, Dunn T. 1997. Hydroxylation of *Saccharomyces cerevisiae* ceramides requires Sur2p and Scs7p. *Journal of Biological Chemistry* 272: 29704–29710.

Huang D, Sun Y, Ma Z, Ke M, Cui Y, Chen Z, Chen C, Ji C, Tran TM, Yang L et al. 2019. Salicylic acid-mediated plasmodesmal closure via Remorin-dependent lipid organization. *Proceedings of the National Academy of Sciences, USA* 116: 21274–21284.

Huby E, Napier JA, Baillieul F, Michaelson LV, Dhondt-Cordelier S. 2020. Sphingolipids: towards an integrated view of metabolism during the plant stress response. *New Phytologist* 225: 659–670.

de Keijzer J, Kieft H, Ketelaar T, Goshima G, Janson ME. 2017. Shortening of microtubule overlap regions defines membrane delivery sites during plant cytokinesis. *Current Biology* 27: 514–520.

Klose C, Ejsing CS, García-Sáez AJ, Kaiser H-J, Sampaio JL, Surma MA, Shevchenko A, Schwille P, Simons K. 2010. Yeast lipids can phase-separate into micrometer-scale membrane domains. *Journal of Biological Chemistry* 285: 30224–30232.

König S, Feussner K, Schwarz M, Kaever A, Iven T, Landesfeind M, Ternes P, Karlovsky P, Lipka V, Feussner I. 2012. Arabidopsis mutants of sphingolipid fatty acid α-hydroxylases accumulate ceramides and salicylates. *New Phytologist* 196: 1086–1097.

Krogh A, Larsson B, von Heijne G, Sonnhammer ELL. 2001. Predicting transmembrane protein topology with a hidden Markov model: application to complete genomes. *Journal of Molecular Biology* 305: 567–580.

Lenarčič T, Albert I, Böhm H, Hodnik V, Pirc K, Zavec AB, Podobnik M, Pahovnik D, Žagar E, Pruitt R et al. 2017. Eudicot plant-specific sphingolipids determine host selectivity of microbial NLP cytolysins. *Science* 358: 1431–1434.

Liang H, Yao N, Song JT, Luo S, Lu H, Greenberg JT. 2003. Ceramides modulate programmed cell death in plants. *Genes & Development* 17: 2636–2641.

Liu N-J, Zhang T, Liu Z-H, Chen X, Guo H-S, Ju B-H, Zhang Y-Y, Li G-Z, Zhou Q-H, Qin Y-M et al. 2020. Phytosphinganine affects plasmodesmata permeability via facilitating PDLP5-stimulated callose accumulation in *Arabidopsis*. *Molecular Plant* 13: 128–143.

Lu S, Wang J, Chitsaz F, Derbyshire MK, Geer RC, Gonzales NR, Gwadz M, Hurwitz DI, Marchler GH, Song JS et al. 2020. CDD/SPARCLE: the conserved domain database in 2020. *Nucleic Acids Research* 48: D265–D268.

Luttgeharm KD, Kimberlin AN, Cahoon EB. 2016. Plant sphingolipid metabolism and function. In: Nakamura Y, Li-Beisson Y, eds. *Lipids in plant and algae development*. Cham: Springer International Publishing, 249–286.

Lynch DV, Dunn TM. 2004. An introduction to plant sphingolipids and a review of recent advances in understanding their metabolism and function. *New Phytologist* 161: 677–702.

Mamode Cassim A, Gouguet P, Gronnier J, Laurent N, Germain V, Grison M, Boutté Y, Gerbeau-Pissot P, Simon-Plas F, Mongrand S. 2019. Plant lipids: Key players of plasma membrane organization and function. *Progress in Lipid Research* 73: 1–27.

Marchler-Bauer A, Derbyshire MK, Gonzales NR, Lu S, Chitsaz F, Geer LY, Geer RC, He J, Gwadz M, Hurwitz DI et al. 2015. CDD: NCBI's conserved domain database. *Nucleic Acids Research* 43: D222–226.

Markham JE, Jaworski JG. 2007. Rapid measurement of sphingolipids from *Arabidopsis thaliana* by reversed-phase high-performance liquid chromatography coupled to electrospray ionization tandem mass spectrometry. *Rapid Communications in Mass Spectrometry* 21: 1304–1314.

Markham JE, Li J, Cahoon EB, Jaworski JG. 2006. Separation and identification of major plant sphingolipid classes from leaves. *Journal of Biological Chemistry* 281: 22684–22694.

Markham JE, Molino D, Gissot L, Bellec Y, Hematy K, Marion J, Belcram K, Palauqui J-C, Satiat-JeuneMaitre B, Faure J-D. 2011. Sphingolipids containing very-long-chain fatty acids define a secretory pathway for specific polar plasma membrane protein targeting in *Arabidopsis*. *Plant Cell* 23: 2362–2378.

Mizutani Y, Kihara A, Igarashi Y. 2004. Identification of the human sphingolipid C4-hydroxylase, hDES2, and its up-regulation during keratinocyte differentiation. *FEBS Letters* 563: 93–97.

Molino D, Van der Giessen E, Gissot L, Hématy K, Marion J, Barthelemy J, Bellec Y, Vernhettes S, Satiat-Jeunemaétre B, Galli T et al. 2014. Inhibition of very long acyl chain sphingolipid synthesis modifies membrane dynamics during plant cytokinesis. *Biochimica et Biophysica Acta* 1841: 1422–1430.

Mombelli E, Morris R, Taylor W, Fraternali F. 2003. Hydrogen-bonding propensities of sphingomyelin in solution and in a bilayer assembly: a molecular dynamics study. *Biophysical Journal* 84: 1507–1517.

Msanne J, Chen M, Luttgeharm KD, Bradley AM, Mays ES, Paper JM, Boyle DL, Cahoon RE, Schrick K, Cahoon EB. 2015. Glucosylceramides are critical for cell-type differentiation and organogenesis, but not for cell viability in Arabidopsis. *The Plant Journal* 84: 188–201.

Mueller AO, Blersch KF, Gippert AL, Ischebeck T. 2017. Tobacco pollen tubes – a fast and easy tool for studying lipid droplet association of plant proteins. *The Plant Journal* 89: 1055–1064.

Mueller SJ, Reski R. 2015. Mitochondrial dynamics and the ER: the plant perspective. *Frontiers in Cell and Developmental Biology* 3: 78.

Ortiz-Ramírez C, Hernandez-Coronado M, Thamm A, Catarino B, Wang M, Dolan L, Feijó JA, Becker JD. 2016. A transcriptome atlas of *Physcomitrella patens* provides insights into the evolution and development of land plants. *Molecular Plant* 9: 205–220.

Pike LJ. 2009. The challenge of lipid rafts. *Journal of Lipid Research* 50(Suppl): S323–S328.

Quinn PJ, Wolf C. 2009. The liquid-ordered phase in membranes. *Biochimica Biophysica Acta* 1788: 33–46.

Rensing SA, Lang D, Zimmer AD, Terry A, Salamov A, Shapiro H, Nishiyama T, Perroud P-F, Lindquist EA, Kamisugi Y et al. 2008. The *Physcomitrella* genome reveals evolutionary insights into the conquest of land by plants. *Science* 319: 64–69.

Resemann HC, Herrfurth C, Feussner K, Hornung E, Ostendorf AK, Gömann J, Mittag J, van Gessel N, de Vries J, Ludwig-Müller J et al. 2021. Convergence of sphingolipid desaturation across over 500 million years of plant evolution. *Nature Plants* 7: 219–232.

Reski R, Abel WO. 1985. Induction of budding on chloronemata and caulonemata of the moss, *Physcomitrella patens*, using isopentenyladenine. *Planta* 165: 354–358.

Schaefer D, Zryd J-P, Knight CD, Cove DJ. 1991. Stable transformation of the moss *Physcomitrella patens*. *Molecular and General Genetics* 226: 418–424.

Scherp P, Grotha R, Kutschera U. 2001. Occurrence and phylogenetic significance of cytokinesis-related callose in green algae, bryophytes, ferns and seed plants. *Plant Cell Reports* 20: 143–149.

Schneider CA, Rasband WS, Eliceiri KW. 2012. NIH Image to ImageJ: 25 years of image analysis. *Nature Methods* 9: 671–675.

Schuette S, Wood AJ, Geisler M, Geisler-Lee J, Ligrone R, Renzaglia KS. 2009. Novel localization of callose in the spores of *Physcomitrella patens* and phylogenomics of the callose synthase gene family. *Annals of Botany* 103: 749–756.

Shanklin J, Cahoon EB. 1998. Desaturation and related modifications of fatty acids. *Annual Review of Plant Physiology and Plant Molecular Biology* 49: 611–641.

Shi L, Bielawski J, Mu J, Dong H, Teng C, Zhang J, Yang X, Tomishige N, Hanada K, Hannun YA *et al.* 2007. Involvement of sphingoid bases in mediating reactive oxygen intermediate production and programmed cell death in *Arabidopsis*. *Cell Research* 17: 1030–1040.

Simons K, Ikonen E. 1997. Functional rafts in cell membranes. *Nature* 387: 569–572.

Simpson C, Thomas C, Findlay K, Bayer E, Maule AJ. 2009. An *Arabidopsis* GPI-anchor plasmodesmal neck protein with callose binding activity and potential to regulate cell-to-cell trafficking. *Plant Cell* 21: 581–594.

Slotte JP. 1999. Sphingomyelin-cholesterol interactions in biological and model membranes. *Chemistry and Physics of Lipids* 102: 13–27.

Slotte JP. 2016. The importance of hydrogen bonding in sphingomyelin's membrane interactions with co-lipids. *Biochimica et Biophysica Acta* 1858: 304–310.

Smith WL, Merrill AH Jr. 2002. Sphingolipid metabolism and signaling minireview series. *Journal of Biological Chemistry* 277: 25841–25842.

Sonnhammer E, von Heijne G, Krogh A. 1998. A hidden Markov model for predicting transmembrane helices in protein sequences. *Proceedings on the International Conference on Intelligent Systems Molecular Biology* 6: 175–182.

Sperling P, Franke S, Luthje S, Heinz E. 2005. Are glucocerebrosides the predominant sphingolipids in plant plasma membranes? *Plant Physiology and Biochemistry* 43: 1031–1038.

Sperling P, Ternes P, Moll H, Franke S, Zähringer U, Heinz E. 2001. Functional characterization of sphingolipid C4-hydroxylase genes from *Arabidopsis thaliana*. *FEBS Letters* 494: 90–94.

Tarazona P, Feussner K, Feussner I. 2015. An enhanced plant lipidomics method based on multiplexed liquid chromatography–mass spectrometry reveals additional insights into cold- and drought-induced membrane remodeling. *The Plant Journal* 84: 621–633.

Tartaglio V, Rennie EA, Cahoon R, Wang G, Baidoo E, Mortimer JC, Cahoon EB, Scheller HV. 2017. Glycosylation of inositol phosphorylceramide sphingolipids is required for normal growth and reproduction in Arabidopsis. *The Plant Journal* 89: 278–290.

Tilsner J, Nicolas W, Rosado A, Bayer EM. 2016. Staying tight: Plasmodesmal membrane contact sites and the control of cell-to-cell connectivity in plants. *Annual Review of Plant Biology* 67: 337–364.

Vatén A, Dettmer J, Wu S, Stierhof YD, Miyashima S, Yadav SR, Roberts CJ, Campilho A, Bulone V, Lichtenberger R *et al.* 2011. Callose biosynthesis regulates symplastic trafficking during root development. *Developmental Cell* 21: 1144–1155.

Winter D, Vinegar B, Nahal H, Ammar R, Wilson GV, Provart NJ. 2007. An "Electronic Fluorescent Pictograph" browser for exploring and analyzing large-scale biological data sets. *PLoS ONE* 2: e718.

Yan D, Liu Y. 2020. Diverse regulation of plasmodesmal architecture facilitates adaptation to phloem translocation. *Journal of Experimental Botany* 71: 2505–2512.

Yanagawa D, Ishikawa T, Imai H. 2017. Synthesis and degradation of long-chain base phosphates affect fumonisin B$_1$-induced cell death in *Arabidopsis thaliana*. *Journal of Plant Research* 130: 571–585.

Zavaliev R, Ueki S, Epel BL, Citovsky V. 2011. Biology of callose (β-1,3-glucan) turnover at plasmodesmata. *Protoplasma* 248: 117–130.

Zienkiewicz A, Gömann J, König S, Herrfurth C, Liu Y-T, Meldau D, Feussner I. 2020. Disruption of Arabidopsis neutral ceramidases 1 and 2 results in specific sphingolipid imbalances triggering different phytohormone-dependent plant cell death programs. *New Phytologist* 226: 170–188.

Supporting Information

Additional Supporting Information may be found online in the Supporting Information section at the end of the article.

Fig. S1 Prediction data for *P. patens* S4H gene expression, functional domains and transmembrane domains.

Fig. S2 *P. patens* S4H localises to the ER in protonema cells and complementation of *S. cerevisiae* sur2Δ with *P. patens* S4H restores formation of trihydroxy LCBs.

Fig. S3 *P. patens* s4h mutant characterisation and ceramide and GlcCer fold changes in s4h lines.

Fig. S4 *P. patens* *s4h-1* and *s4h-2* have altered GIPC profiles.

Fig. S5 Series B GIPCs strongly accumulate in *P. patens* *s4h-1* and *s4h-2*.

Fig. S6 Molecular species with unhydroxylated fatty acids accumulate in *P. patens* *s4h-1* and *s4h-2*.

Fig. S7 Total levels of SG are not affected in *P. patens* *s4h-1* and *s4h-2*.

Fig. S8 Dry weight protonema biomass of *P. patens* wild-type, *s4h-1* and *s4h-2*.

Table S1 Gene-specific primers (fw – forward, rev – reverse) used for homologous recombination.

Table S2 Gene-specific primers (fw – forward, rev – reverse) used for characterisation of targeted gene disruption.

Table S3 Gene-specific primers (fw – forward, rev – reverse) used for reverse transcriptase PCR.

Table S4 Gene-specific primers (fw – forward, rev – reverse) used for cloning of subcellular localisation construct of PpS4H.

Table S5 Gene-specific primers (fw – forward, rev – reverse) used for *S. cerevisiae* complementation.

Tables S6 Raw data (absolute) from sphingolipid and sterol analysis in *P. patens*.

Tables S7 Raw data (relative) from sphingolipid and sterol analysis in *P. patens*.

Please note: Wiley Blackwell are not responsible for the content or functionality of any Supporting Information supplied by the authors. Any queries (other than missing material) should be directed to the *New Phytologist* Central Office.

About *New Phytologist*

- *New Phytologist* is an electronic (online-only) journal owned by the New Phytologist Foundation, a **not-for-profit organization** dedicated to the promotion of plant science, facilitating projects from symposia to free access for our Tansley reviews and Tansley insights.

- Regular papers, Letters, Viewpoints, Research reviews, Rapid reports and both Modelling/Theory and Methods papers are encouraged. We are committed to rapid processing, from online submission through to publication 'as ready' via *Early View* – our average time to decision is <26 days. There are **no page or colour charges** and a PDF version will be provided for each article.

- The journal is available online at Wiley Online Library. Visit **www.newphytologist.com** to search the articles and register for table of contents email alerts.

- If you have any questions, do get in touch with Central Office (np-centraloffice@lancaster.ac.uk) or, if it is more convenient, our USA Office (np-usaoffice@lancaster.ac.uk)

- For submission instructions, subscription and all the latest information visit **www.newphytologist.com**